

# What powers the most relativistic jets? – II. Flat-spectrum radio quasars

Emma Gardner<sup>★</sup> and Chris Done<sup>★</sup>

*Centre for Extragalactic Astronomy, Department of Physics, University of Durham, South Road, Durham DH1 3LE, UK*

Accepted 2017 September 25. Received 2017 September 5; in original form 2017 July 16

## ABSTRACT

Flat-spectrum radio quasars (FSRQs) are the most powerful relativistic jets seen from supermassive black holes (BHs) accreting via a radiatively efficient thin disc. Their high energy emission is well modelled by highly relativistic electrons in the jet Compton upscattering an external source of seed photons, primarily from the broad-line region. Strong Doppler boosting by the jet bulk motion makes these FSRQs readily detectable by the *Fermi* Large Area Telescope. We combine jet spectral models with scaling relations for the jet physical parameters as a function of mass and accretion rate. This does not match well to the gamma-ray loud narrow-line Seyfert 1s, assuming their low BH masses are reliable, but is able to predict much of the spectral evolution observed along the Blazar sequence. We use these models in conjunction with cosmological simulations of efficiently accreting BH number densities, and find that they overpredict the observed number of FSRQs by two orders of magnitude if all of these objects produce an FSRQ jet. We can better reproduce the observed numbers if jets are only produced by high-spin BHs and BH spin is built from chaotically aligned accretion episodes so that high-spin BHs are rare. However, this does not reproduce the observed redshift and mass accretion rate distributions of the FSRQs. This may indicate a redshift dependence in accretion mode, with sustained alignment accretion episodes being more prevalent at higher redshift, or that there is some other trigger for FSRQ jets.

**Key words:** accretion, accretion discs – black hole physics – galaxies: jets – quasars: supermassive black holes – cosmology: miscellaneous – gamma-rays: galaxies.

## 1 INTRODUCTION

Blazars are the most extreme examples of relativistic jets from supermassive black holes (BHs). They represent a class of active galactic nuclei (AGN), where the jet is highly relativistic ( $\Gamma > 10$ ) and closely aligned with our line of sight. The jet emission is strongly Doppler boosted by the relativistic bulk motion and consequently dominates the spectrum of the AGN, from radio up to gamma-rays. As a result, these are the most numerous sources detected by the *Fermi*/LAT satellite in the GeV regime (Nolan et al. 2012).

Blazars can be divided into two types – BL Lacs and flat-spectrum radio quasars (FSRQs). This division is made on an arbitrary upper limit to the observed equivalent width of the emission lines, but this typically correlates with the broad-band continuum properties, where the jet spectra of BL Lacs consist of a low-energy hump from synchrotron emission and a second, similar luminosity higher energy hump from synchrotron self-Compton (SSC) emission. The spectra of FSRQ jets also show a low-energy peak from synchrotron emission but have a much more luminous Compton hump, often by more than an order of magnitude (Fossati et al. 1998). This can be explained by there being an intrinsic difference between the

majority of BL Lacs and FSRQs (a small fraction of objects are misclassified due to selection effects: Giommi et al. 2012), such that the BL Lacs do not have additional seed photons from outside of the jet. In contrast, the FSRQs have a disc and associated broad-line region (BLR), which provide an additional external source of seed photons for Compton scattering, leading to the observed Compton peak dominance in FSRQs (e.g. Ghisellini et al. 2017).

This change in seed photons plausibly occurs because of a change in the accretion mode similar to that seen in the black hole binary systems (see e.g. Done, Gierliński & Kubota 2007). FSRQs are high accretion rate AGN containing highly accreting BHs ( $\dot{m} = \dot{M}/\dot{M}_{\text{Edd}} > 0.01$ , where  $\eta\dot{M}_{\text{Edd}}c^2 = L_{\text{Edd}}$ ). At high accretion rates, the accretion flow around the BH takes the form of a radiatively efficient accretion disc, which can often be seen dominating in the optical-UV in FSRQ spectra, despite the strong jet emission (Ghisellini et al. 2010, hereafter G10). The strong UV disc emission illuminates material above the disc, which at a particular radius, set by the gas density and illuminating flux, re-emits the radiation in the form of broad emission lines (the ‘broad-line region’). Some fraction of the accretion disc emission is also reprocessed by the torus. Together, the UV bright accretion disc, BLR and reprocessed emission from the torus all act as sources of external seed photons for the jet. However, crucially, the radius at which the broad lines are produced is normally at a larger distance from the BH than the region of the jet where the high energy emission is produced

\* E-mail: e.l.gardner@dur.ac.uk (EG); chris.done@durham.ac.uk (CD)

(Ghisellini & Tavecchio 2009). As a result, the jet electrons moving with the relativistic bulk motion of the jet see the stationary BLR seed photons strongly Doppler boosted and this greatly enhances the external Compton emission of the FSRQ.

In contrast, the BHs responsible for the production of BL Lac jets are at much lower accretion rates ( $\dot{m} < 0.01$ ), where the accretion flow switches from a geometrically thin, radiatively efficient UV bright disc to a hotter, geometrically thick, radiatively inefficient flow (e.g. Advection Dominated Accretion Flow: ADAF Narayan & Yi 1995). The switch to a radiatively inefficient accretion flow means there is no UV bright inner disc to illuminate the BLR and provide external seed photons. As a result, BL Lac spectra lack both disc emission and broad lines (Stickel et al. 1991) and their high energy Compton humps include only SSC of synchrotron emission generated intrinsically within the jet (Ghisellini, Maraschi & Tavecchio 2009). For the remainder of this paper, we assume all objects with  $\dot{m} \geq 0.01$  have a disc/BLR/torus and refer to these as FSRQs, whilst those with  $\dot{m} < 0.01$  have none of these external components and we refer to these as BL Lacs.

Whilst the mechanisms by which blazar jets emit radiation are relatively well understood, where the energy comes from to power these jets in the first place is not. These jets have bulk Lorentz factors of 10–15 and estimates of the jet power in FSRQs put it at the order of the accretion power or above (G10; Ghisellini et al. 2014). This requires tapping the spin energy of the BH (Blandford & Znajek 1977) and means that the most relativistic jets should necessarily be produced by the most highly spinning BHs.

Gardner & Done (2014, hereafter Paper 1) took a statistical approach to this problem. Rather than studying individual sources, Paper 1 concentrated on modelling the population of *Fermi* blazars as a whole – specifically the population of BL Lacs, since they do not have the added complication of external seed photon sources. Cosmological simulations predict the number of BHs accreting at each redshift as a function of mass and accretion rate. Since BL Lac jets are produced when  $\dot{m} < 0.01$ , they should only be produced by low accretion rate BHs. Paper 1 initially assumed that all BHs with  $\dot{m} < 0.01$  produced a BL Lac type jet. The predicted numbers of these BHs were taken from the Millennium Simulation (Springel et al. 2005; Fanidakis et al. 2011, 2012) and each BH was then assigned a jet spectrum, appropriately scaled to its mass and accretion rate, assuming all size scales in the jet scale with BH mass and the power in particles and jet magnetic fields is a fixed fraction of the accretion power. Each jet was then given a random orientation and its resulting redshifted flux calculated to determine whether it would be bright enough to be detected by *Fermi*. This predicted population of *Fermi*-detected BL Lacs was found to overpredict the observed number of *Fermi*-detected BL Lacs by three orders of magnitude. Producing a BL Lac jet requires a BH with  $\dot{m} < 0.01$ , but clearly not every BH with  $\dot{m} < 0.01$  produces a BL Lac jet (see e.g. Wilson & Colbert 1995; Moderski, Sikora & Lasota 1998; Padovani et al. 2015).

Paper 1 found that the observed number of BL Lacs was much better reproduced if production of BL Lac jets was restricted to BHs with  $\dot{m} < 0.01$  and high spin ( $a > 0.8$ ). Maraschi et al. (2012) argue that the efficiency of spin-powered jet production drops off sharply below 0.8, so that this forms an effective spin threshold for relativistic jet production. This reduces the predicted population sufficiently if high-spin BHs are rare. Aligned accretion is very efficient at spinning up the BH (e.g. Volonteri, Sikora & Lasota 2007). However, randomly aligned small accretion episodes (chaotic accretion) result in low spin (King, Pringle & Hofmann 2008), with high-spin BHs produced only through BH–BH mergers (Fanidakis

et al. 2011, 2012). Restricting production of BL Lac jets to high-spin, low accretion rate BHs and assuming chaotic accretion not only allows the total number of *Fermi*-detected BL Lacs to be reproduced but also better matches the observed mass and redshift distributions. This is because the low accretion rate, high-spin BHs are those that are formed latest in gas-poor mergers that produce the most massive BHs. This suggests that high spin may be required to produce the highly relativistic jets in BL Lacs.

In this paper, we use the same method to try to predict the observed population of *Fermi*-detected FSRQs. The scaling relations are able to reproduce the FSRQ blazar sequence with increasing BH mass (Ghisellini et al. 2017), but the small population of gamma-ray loud NLS1s ( $\gamma$ NLS1s) are more Compton dominant than standard jet scaling relations predict. This suggests that either FSRQ jets do not follow standard jet scaling relations, or  $\gamma$ NLS1 masses may be larger than previously estimated, as has been suggested by Calderone et al. (2013), Baldi et al. (2016) and D’Ammando et al. (2017).

We again use the BH number densities predicted by the Millennium Simulation and this time assume that all BHs accreting with  $\dot{m} > 0.01$  produce an FSRQ type jet. We extend the spectral model of Paper 1 to include external sources of seed photons and assume the same standard jet scalings (size scales scale with  $M_{\text{BH}}$  and power in particles and magnetic fields scales with accretion power), which mimic the observed spectral changes in BL Lacs (Paper 1). As in Paper 1, we find that assuming all BHs in the appropriate accretion regime produce a highly relativistic jet overpredicts the observed FSRQ population, however by not as much (only two orders of magnitude, rather than three in the case of BL Lacs). Again, we try imposing a spin cut, such that only high spin, high accretion rate BHs produce FSRQ jets. However, although this allows us to better match the observed number of *Fermi*-detected FSRQs, we find we cannot match the observed mass, accretion rate or redshift distributions – particularly the tail out to high redshifts ( $z > 2$ ). This is due to a lack of high-mass, high-spin BHs in the cosmological simulations at redshift 2–3. If production of an FSRQ jet really does require a high-spin BH, our simulations suggest there should be more high-mass, high-spin BHs at high redshift than a solely chaotic accretion model predicts. This suggests that there may be a trend from chaotic accretion towards more prolonged accretion (which spins up rather than spins down the BH) at higher redshifts, as also suggested by Dotti et al. (2013) and Dubois, Volonteri & Silk (2014).

## 2 EXTERNAL-COMPTON JETS

We extend the single-zone SSC model of Paper 1 to include sources of external seed photons, since these are important in the higher accretion rate FSRQs, which have UV bright accretion discs. We code up the model of Ghisellini & Tavecchio (2009), including seed photons from the accretion disc and X-ray corona, emission from the BLR and torus, and reflection of coronal X-rays off the BLR. We follow their notation below, where quantities in the jet frame are primed when there could be confusion, but not where it is self-evident, e.g. jet quantities such as electron Lorentz factors and jet magnetic field.

We have made this code publicly available within the XSPEC spectral fitting package. We briefly summarize the model here, with full details in the Appendix.

We assume a spherical emission region of radius  $R_{\text{diss}}$  and a conical jet, such that  $R_{\text{diss}}$  is related to the distance of the emission

region from the BH by  $R_{\text{diss}} = \phi Z_{\text{diss}}$ , where  $\phi$  is the half opening angle of the jet. We assume the jet emission is dominated by this single spherical emission region at the jet base and neglect the contribution from regions further out along the jet, as this mostly affects the low-energy (predominantly radio) emission. We assume material in the jet moves at a constant bulk Lorentz factor ( $\Gamma$ ), and that a fraction of the resulting jet power is used to accelerate electrons in the emission region. The power injected into relativistic electrons in the jet frame is then  $P'_{\text{rel}} = 4/3\pi R_{\text{diss}}^3 \int \gamma m_e c^2 Q(\gamma) d\gamma$ , where the accelerated electron distribution is a broken power law of the form:

$$Q(\gamma) = Q_0 \frac{\left(\frac{\gamma}{\gamma_b}\right)^{-s_1}}{\left[1 + \left(\frac{\gamma}{\gamma_b}\right)^{-s_1+s_2}\right]} \quad (1)$$

for  $\gamma_{\text{min}} < \gamma < \gamma_{\text{max}}$ .

We note that this is slightly different from the form used in Paper 1. First, we now use  $s$  rather than  $n$  to denote the injected power-law indices in order to be consistent with Ghisellini & Tavecchio (2009). Secondly, Paper 1 has the denominator as  $(1 - \gamma/\gamma_b)^{-s_1+s_2}$  rather than the form used here and in Ghisellini & Tavecchio (2009). We have run tests and find that this change generally gives less than a factor 30 per cent difference in the resultant spectra.

These electrons cool by emitting self-absorbed synchrotron and SSC radiation and by upscattering seed photons from external sources of radiation. We assume the distance of the BLR and infra-red torus ( $R_{\text{BLR}}$  and  $R_{\text{IR}}$ ) from the central BH scale with the accretion disc luminosity as (Ghisellini & Tavecchio 2009)

$$R_{\text{BLR}} = 10^{17} \left(\frac{L_d}{10^{45} \text{ erg s}^{-1}}\right)^{1/2} \text{ cm}, \quad (2)$$

$$R_{\text{IR}} = 2.5 \times 10^{18} \left(\frac{L_d}{10^{45} \text{ erg s}^{-1}}\right)^{1/2} \text{ cm}. \quad (3)$$

The total seed photon energy density in the jet frame is  $U'_{\text{seed}} = U'_B + g(\gamma)(U'_{\text{sync}} + U'_{\text{ex}})$  and therefore includes both the magnetic energy density,  $U'_B = B^2/8\pi$ , and the fraction  $g(\gamma)$  of the energy density of synchrotron,  $U'_{\text{sync}}$ , and external,  $U'_{\text{ex}}$ , seed photons which can be Compton upscattered by electrons of energy  $\gamma$  within the Klein–Nishina limit. The accelerated electron distribution cools into a steady-state electron distribution,  $N(\gamma) = -\dot{\gamma}^{-1} \int_{\gamma}^{\gamma_{\text{max}}} Q(\gamma_i) d\gamma_i$ , where the rate at which an electron loses energy is  $\dot{\gamma} m_e c^2 = 4/3\gamma^2 \sigma_T c U'_{\text{seed}}$ . Since the cooling time-scale  $t_{\text{cool}} = \gamma/\dot{\gamma}$  depends on  $\gamma$ , with high-energy electrons cooling fastest, we calculate the electron Lorentz factor that can just cool in a light crossing time of the region,  $\gamma_{\text{cool}}$ , and join smoothly on to the accelerated uncooled electron distribution below this. The full self-consistent electron distribution is then characterized by  $N(\gamma) = Kn(\gamma)$ , where  $K$  is the number density of electrons at  $\gamma = 1$  and  $n(\gamma)$  incorporates all the spectral shape. We calculate the resulting (self-absorbed) synchrotron and Compton emission using the delta function approximation as this is much faster than using the full kernel but is accurate enough for our statistical analysis (Dermer & Menon 2009).

This jet frame emission is boosted by the bulk motion of the jet, where the Doppler factor of the boosting ( $\delta$ ) depends on both  $\Gamma$  and the orientation of the jet as  $\delta = (\Gamma - \cos\theta\sqrt{\Gamma^2 - 1})^{-1}$  and we transform jet frame frequencies ( $\nu'$ ) and luminosities ( $L'$ ) to observed frame quantities as  $\nu = \delta\nu'$  and  $L = \delta^3 L'$ . Dermer &

Menon (2009) advocate multiplying by an additional factor of  $\delta$  for the special case of a seed photon source that is ahead of the jet emission region, to account for the anisotropy in the seed photon field in the jet frame. However, an anisotropic seed photon field produces anisotropic cooling and therefore an anisotropic electron distribution, which can effectively cancel out the effects of the seed photon anisotropy (Ghisellini, George & Done 1989; Ghisellini et al. 1991; Gierliński et al. 1999), assuming that the electrons are not re-isotropized by turbulent scattering on time-scales much shorter than the cooling time. Since we include cooling from multiple seed photons sources (accretion flow, BLR and torus), with multiple orientations with respect to the jet producing multiple anisotropies, we choose to adopt  $\nu = \delta\nu'$  and  $L = \delta^3 L'$  in all cases.

Finally, the jet emission is cosmologically redshifted and attenuated due to pair production on the extragalactic infra-red background light (though this is generally small for the *Fermi* bandpass) to produce the observed flux.

The parameters of our model are therefore as follows:

- (i) Parameters of the accretion flow: BH mass and Eddington scaled accretion rate ( $M_{\text{BH}}$  and  $\dot{m}$ ), for calculating the density of external seed photons.
- (ii) Physical parameters of the jet:  $\Gamma$ , radius of emission region ( $R_{\text{diss}}$ ) and half opening angle of the jet ( $\phi$ ).
- (iii) The magnetic field of the emission region and power injected into relativistic electrons ( $B$  and  $P'_{\text{rel}}$ ).
- (iv) Parameters of the injected electron distribution:  $\gamma_{\text{min}}$ ,  $\gamma_b$ ,  $\gamma_{\text{max}}$ ,  $s_1$  and  $s_2$ .

We adopt the cosmology used in the Millennium simulations:  $h = 0.72$ ,  $\Omega_m = 0.25$ ,  $\Omega_{\text{vac}} = 0.75$  (Springel et al. 2005; Fanidakis et al. 2011).

### 3 SCALING JETS

As in Paper 1, we assume that the acceleration mechanism is the same for all FSRQs, giving the same injected electron distribution, regardless of mass and accretion rate. We also assume all jets are produced with the same  $\Gamma$  and the same half opening angle (which we fix to  $\phi = 0.1$ ). This leaves three remaining parameters:  $R_{\text{diss}}$ ,  $B$  and  $P'_{\text{rel}}$ .

We assume that FSRQs follow the same standard jet scalings that BL Lacs appear to follow (Paper 1). Hence, we scale  $R_{\text{diss}} \propto M$ , since all size scales should scale with the mass of the BH (Heinz & Sunyaev 2003), and assume the jet power is a constant fraction of the total accretion power,  $P_j \propto \dot{m}M$ . We again stress that this assumption is valid whether the jet is powered by the accretion flow or the spin energy of the BH, since extraction of BH spin energy relies on magnetic fields generated in the accretion flow, which will be affected by accretion rate. A constant fraction of the total jet power is then injected into relativistic particles and magnetic fields. Hence,  $P'_{\text{rel}} \propto P_j \propto \dot{m}M$  and  $B \propto U_B^{1/2} \propto (P'_B/R_{\text{diss}}^2)^{1/2} \propto (P_j/R_{\text{diss}}^2)^{1/2} \propto (\dot{m}/M)^{1/2}$  (Paper 1).

We choose the mean FSRQ parameters from G10 to scale from, which are the logarithmic average values from their sample of 53 *Fermi*-detected FSRQs. This gives  $M_0 = 1 \times 10^9 M_{\odot}$ ,  $\dot{m} = 0.1$ ,  $R_0 = 1.89 \times 10^{16}$  cm,  $B_0 = 2.6$  G,  $P'_{\text{rel},0} = 2 \times 10^{43}$  erg s $^{-1}$ ,  $\Gamma = 13$ ,  $\gamma_{\text{min}} = 1$ ,  $\gamma_b = 300$ ,  $\gamma_{\text{max}} = 3 \times 10^3$ ,  $s_1 = 1$ ,  $s_2 = 2.7$ , and we scale  $R_{\text{diss}}$ ,  $P'_{\text{rel}}$  and  $B$  as

$$R_{\text{diss}} = R_0 \frac{M}{M_0} \quad (4)$$

$$P'_{\text{rel}} = P'_{\text{rel},0} \frac{\dot{m}}{\dot{m}_0} \frac{M}{M_0} \quad (5)$$

$$B = B_0 \left( \frac{\dot{m}}{\dot{m}_0} \frac{M}{M_0} \right)^{1/2}. \quad (6)$$

The distance to the BLR and IR torus are both  $\propto L_d^{1/2}$ . This implies  $R_{\text{BLR}}$  and  $R_{\text{IR}}$  should also scale with the mass and accretion rate of the BH, since  $L_d \propto \dot{m} M$ . Hence,  $R_{\text{BLR}} \propto R_{\text{IR}} \propto (\dot{m} M)^{1/2}$ .

### 3.1 Spectral changes with mass

Fig. 1(a) shows a sequence of FSRQ spectra with increasing BH mass. The accretion rate is fixed to  $\dot{m} = 0.1$  and  $R_{\text{diss}}$ ,  $B$  and  $P'_{\text{rel}}$  are scaled as described above.

As BH mass decreases, so does the size of the emission region, since  $R_{\text{diss}} \propto M$ . This can be seen in the increase in synchrotron self-absorption frequency, from  $\sim 10^{10.5}$  (black spectrum) to  $\sim 10^{11.5}$  (magenta spectrum). The total luminosity also decreases, since the power injected into relativistic electrons decreases with decreasing mass ( $P'_{\text{rel}} \propto M$ ).

The relative strengths of the synchrotron and Compton humps also changes with mass. The blue spectrum corresponds to the mean FSRQ model of G10, with  $\dot{m} = 0.1$ ,  $M = 10^9 M_{\odot}$ . It shows a strong Compton hump at  $10^{22}$  Hz due to Compton up-scattering of external seed photons, predominantly from the BLR. The low-energy synchrotron hump is roughly an order of magnitude less luminous ( $\sim 10^{46}$  erg s $^{-1}$ ). As the BH mass drops from  $10^9$  (blue) to  $10^6 M_{\odot}$  (magenta), the relative luminosity of the Compton hump decreases until at the lowest masses the two humps show comparable luminosity. The relative strength of the two humps depends on the relative strength of the energy density in magnetic fields compared to the energy density of external seed photons.

Fig. 1(b) shows the spectral energy density of seed photons in the jet frame. As mass drops so does the emission region size and hence its distance from the BH, since  $Z_{\text{diss}} = R_{\text{diss}}/\phi \propto M$ . Smaller  $Z_{\text{diss}}$  increases the energy density of accretion disc seed photons, despite the drop in  $L_d$  with  $M$ , showing an increase of approximately three orders of magnitude (blue dashed line to magenta dashed line). However, the dominant source of seed photons is  $U'_{\text{BLR}}$  and this stays constant, since  $U'_{\text{BLR}} \propto L_d/R_{\text{BLR}}^2 \propto L_d/(L_d^{1/2})^2 = \text{const}$  for  $Z_{\text{diss}} < R_{\text{BLR}}$  (blue dot-dashed line). In contrast, the magnetic field, which determines the amount of synchrotron emission, increases as BH mass decreases, since  $B \propto M^{-1/2}$ . As a result,  $U'_{\text{sync}}$  (solid lines) increases by more than four orders of magnitude, becoming comparable to  $U'_{\text{BLR}}$  at the lowest masses. Consequently, the Compton humps of the lowest mass spectra are dominated by up-scattering of synchrotron radiation, causing them to look more like low accretion rate SSC BL Lacs than FSRQs, despite their higher accretion rates.

The lack of external seed photons means less efficient cooling in lower mass objects. For the  $10^9 M_{\odot}$  spectrum (Fig. 1a, blue line), the cooling is almost complete with  $\gamma_{\text{cool}} = 7$ , where  $\gamma_{\text{cool}}$  is the minimum Lorentz factor of electrons that can cool in one light crossing time. For the  $10^6 M_{\odot}$  spectrum (magenta),  $\gamma_{\text{cool}}$  has increased to  $10^6$ , resulting in a clear spectral break at  $\sim 10^{13.5}$  Hz in the synchrotron emission. The decreasing frequency of this spectral break tracks the decrease in  $\gamma_{\text{cool}}$  and increase in cooling from  $10^6$  to  $10^9 M_{\odot}$ .

Above  $10^9 M_{\odot}$ ,  $\gamma_{\text{cool}}$  increases again (Fig. 1a, black spectrum,  $\gamma_{\text{cool}} = 39$ ). This is because for a  $10^{10} M_{\odot}$  BH the emission region has gone beyond  $R_{\text{BLR}}$ , since  $Z_{\text{diss}} \propto M$  whilst  $R_{\text{BLR}}$  (and  $R_{\text{IR}} \propto$

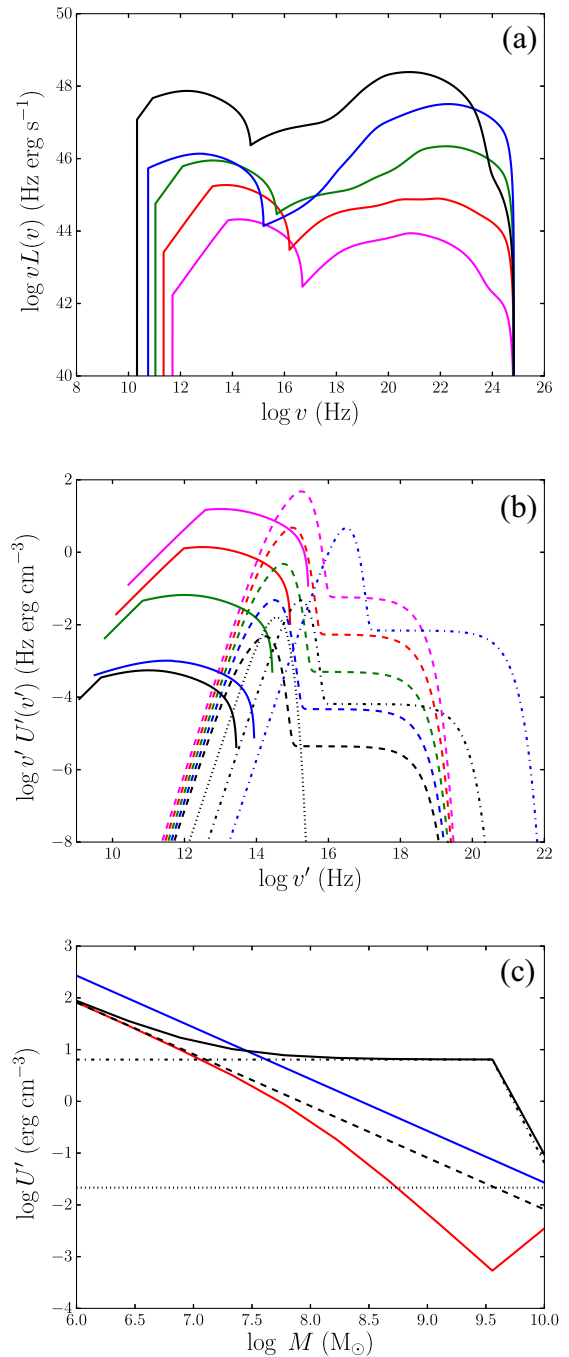


**Figure 1.** Spectral changes with mass using standard jet scalings ( $R_{\text{diss}} \propto M$ ,  $P'_{\text{rel}} \propto \dot{m} M$ ,  $B \propto (\dot{m}/M)^{1/2}$ ). (a) FSRQ model SEDs for fixed accretion rate and increasing BH mass ( $M_{\text{BH}} = 10^6$  (magenta),  $10^7$  (red),  $10^8$  (green),  $10^9$  (blue) and  $10^{10} M_{\odot}$  (black),  $\dot{m} = 0.1$ ). (b) Corresponding seed photon energy density spectra as seen in the jet frame. Solid lines show synchrotron seed photons, dashed lines show accretion disc plus coronal seed photons, dot-dashed lines show seed photons from the BLR plus coronal flux reflected by the BLR, and dotted lines show seed photons from the torus. The seed photon energy density from the torus is the same for all masses. The seed photon energy density from the BLR is the same for all masses except  $10^{10} M_{\odot}$ , where  $Z_{\text{diss}} > R_{\text{BLR}}$ . (c) Seed photon energy densities in jet frame as a function of BH mass. Blue line shows  $U'_B$ , red line shows  $U'_{\text{sync}}$ . Black lines show energy densities of external seed photons, where dashed line shows  $U'_d + U'_X$ , dot-dashed line shows  $U'_{\text{BLR}} + U'_{\text{XBLR}}$ , dotted line shows  $U'_{\text{IR}}$  and solid line shows total  $U'_{\text{ex}}$ .

$M^{1/2}$ . This causes  $U'_{\text{BLR}}$  to drop dramatically (black dot–dashed line in Fig. 1c), reducing the amount of cooling. The next strongest source of seed photons is the torus (Fig. 1b, black dotted line).  $U'_{\text{IR}}$  is constant for all masses since like  $U'_{\text{BLR}}$ ,  $U'_{\text{IR}} \propto L_d/R_{\text{IR}}^2 \propto L_d/(L_d^{1/2})^2 = \text{const}$  for  $Z_{\text{diss}} < R_{\text{IR}}$ , which is the case for all five masses. Consequently, above  $10^9 M_{\odot}$  the ratio between synchrotron and Compton peaks drops again.

Fig. 1(c) shows the total energy densities of seed photons in the jet frame as a function of BH mass. This shows clearly for masses around  $10^9 M_{\odot}$ , where the energy density of BLR photons dominates (black dot–dashed line), the energy density of synchrotron radiation is suppressed (red line) due to the strong cooling.  $U'_{\text{sync}}$  recovers at higher masses as  $Z_{\text{diss}} > R_{\text{BLR}}$  and dominates over  $U'_{\text{BLR}}$  at low masses ( $< 10^7 M_{\odot}$ ), where the magnetic field is strongest (blue line).

The sequence of spectra shown in Fig. 1(a) appear remarkably similar to the sequence of observed FSRQ spectra binned by luminosity shown by Ghisellini et al. (2017). Ghisellini et al. (2017) find that the Compton dominance of FSRQ spectra increases with luminosity, causing the X-ray spectral slope to harden. Fig. 1(a) shows that this can be explained if the higher luminosity bins are dominated by increasingly higher mass FSRQs.

### 3.2 Spectral changes with accretion rate

Fig. 2(a) shows a sequence of FSRQ spectra with increasing accretion rate. We fix  $M = 10^9$  and increase the accretion rate from  $\log \dot{m} = -2$  to 0.5, scaling  $R_{\text{diss}}$ ,  $B$  and  $P'_{\text{rel}}$  as described in Section 3.

As accretion rate increases, the synchrotron frequency increases from  $\sim 10^{10}$  (magenta) to  $10^{12}$  Hz (blue). This is because the size of the emission region stays constant ( $R_{\text{diss}}$  does not depend on  $\dot{m}$ ), whilst the magnetic field is increasing ( $B \propto \dot{m}^{1/2}$ ).

As accretion rate increases, the total luminosity also increases, since  $P'_{\text{rel}} \propto \dot{m}$  and  $B \propto \dot{m}^{1/2}$ . However, the synchrotron emission increases faster than the Compton emission, so that the two peaks show comparable luminosity for the highest accretion rate spectrum ( $\log \dot{m} = 0.5$ ; blue), whilst the Compton peak is approximately two orders of magnitude brighter than the synchrotron peak at  $\log \dot{m} = -1.5$  (red).

This is because the increase in synchrotron emission comes from both the increase in  $P'_{\text{rel}}$  and the increase in its seed photons from the magnetic field. In contrast, the main source of seed photons for the Compton hump is the BLR and the energy density of BLR seed photons remains constant, whilst  $Z_{\text{diss}} < R_{\text{BLR}}$ . Hence, most of the increase in  $L_{\text{comp}}$  is due to  $P'_{\text{rel}}$ . Only for the highest accretion rates (blue and cyan spectra), do the other sources of seed photons ( $U'_{\text{sync}}$  and  $U'_{\text{acc}}$ , solid and dashed lines in Fig. 2b) become comparable with  $U'_{\text{BLR}}$ . These are much lower energy photons than the blue shifted BLR emission (Fig. 2b). Consequently, the Compton hump at the highest accretion rates is much broader, as well as being more similar in luminosity to the synchrotron peak. Again this gives a spectral shape much more typical of low accretion rate BL Lacs, except now it is the result of an extremely high  $\dot{m}$  causing  $U'_{\text{sync}}$  to dominate over  $U'_{\text{ex}}$ , rather than (in the case of BL Lacs) an extremely low  $\dot{m}$  where  $U'_{\text{ex}}$  is absent.

The red spectrum in Fig. 2(a) ( $\log \dot{m} = -1.5$ ) shows the greatest luminosity difference between synchrotron and Compton peaks. The difference lessens again for the lowest accretion rate spectrum (magenta,  $\log \dot{m} = -2$ ). This is because  $R_{\text{BLR}} \propto L_d^{1/2} \propto \dot{m}^{1/2}$ . For a  $10^9 M_{\odot}$  BH at  $\dot{m} = 10^{-2}$ , the BLR radius has shrunk so much that it is now less than the distance to the jet emission region. Once

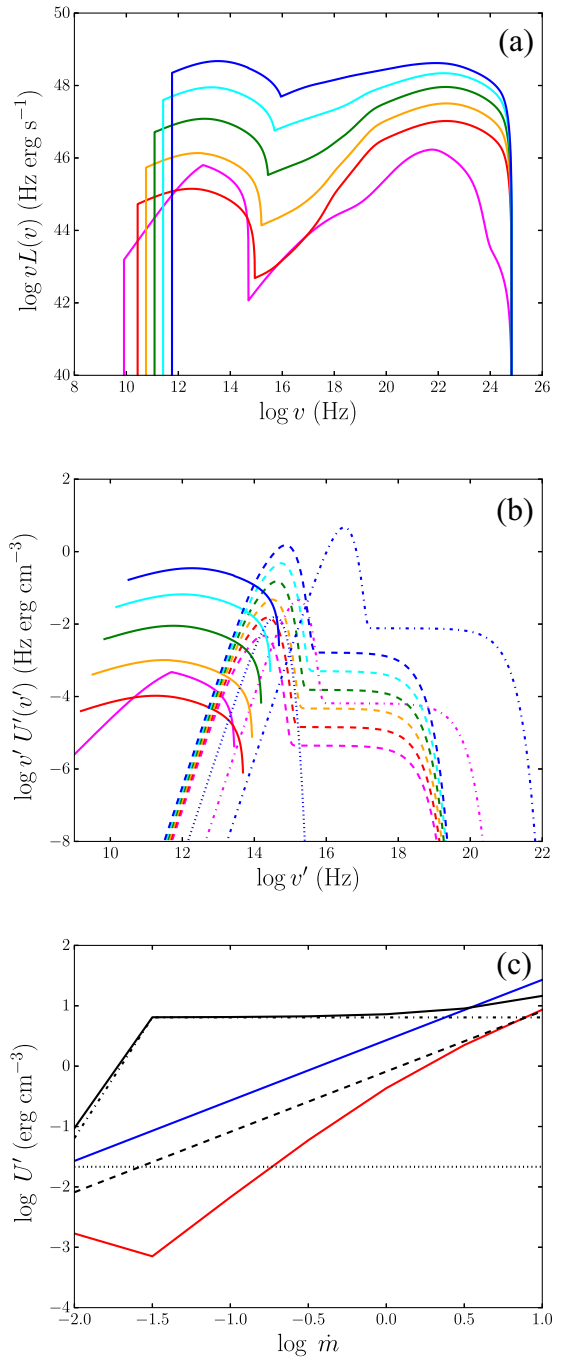


**Figure 2.** Spectral changes with accretion rate using standard jet scalings ( $R_{\text{diss}} \propto M$ ,  $P'_{\text{rel}} \propto \dot{m} M$ ,  $B \propto (\dot{m}/M)^{1/2}$ ). (a) FSRQ model SEDs for fixed BH mass and increasing accretion rate ( $\log \dot{m} = -2$  (magenta),  $-1.5$  (red),  $-1$  (orange),  $-0.5$  (green),  $0$  (cyan) and  $0.5$  (blue),  $M_{\text{BH}} = 10^9 M_{\odot}$ ). (b) Corresponding seed photon energy density spectra as seen in the jet frame. Solid lines show synchrotron seed photons, dashed lines show accretion disc plus coronal seed photons, dot-dashed lines show seed photons from the BLR plus coronal flux reflected by the BLR, and dotted lines show seed photons from the torus. The seed photon energy density from the torus is the same for all accretion rates. The seed photon energy density from the BLR is the same for all accretion rates except  $\log \dot{m} = -2$ , where  $Z_{\text{diss}} > R_{\text{BLR}}$ . (c) Seed photon energy densities in jet frame as a function of accretion rate. Blue line shows  $U'_B$ , red line shows  $U'_{\text{sync}}$ . Black lines show energy densities of external seed photons, where dashed line shows  $U'_d + U'_X$ , dot-dashed line shows  $U'_{\text{BLR}} + U'_{\text{XBLR}}$ , dotted line shows  $U'_{\text{IR}}$  and solid line shows total  $U'_{\text{ex}}$ .

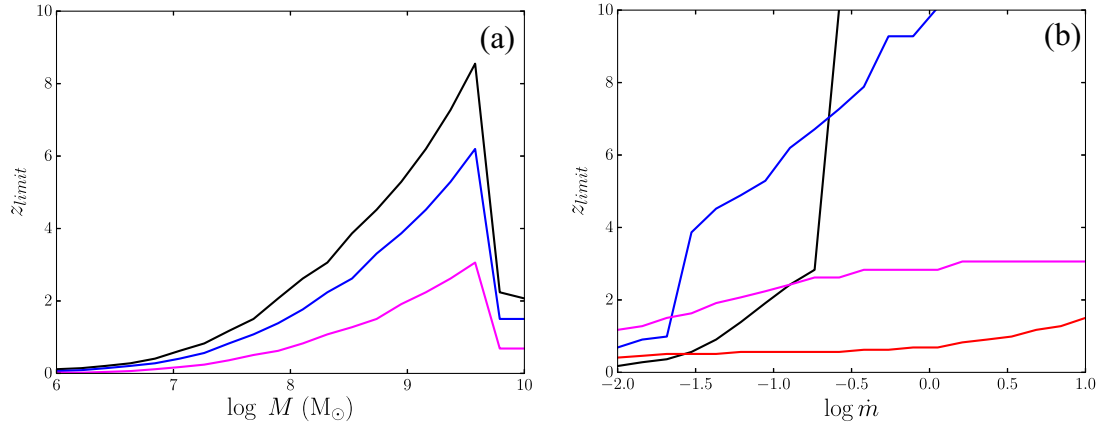


**Figure 3.** (a) Redshift limits for *Fermi* visible FSRQs as a function of BH mass, for increasing viewing angle ( $\theta = 0$  (black),  $1/\Gamma$  (blue) and  $1/2\Gamma$  (magenta), where  $\Gamma = 13$ ) and  $\dot{m} = 0.1$ . (b) Redshift limits for *Fermi* visible FSRQs as a function of accretion rate, for  $M_{\text{BH}} = 10^7$  (red),  $10^8$  (magenta),  $10^9$  (blue) and  $10^{10} M_{\odot}$  (black) and  $\theta = 0$ .

the BLR is behind the jet emission region, its seed photons are deboosted and  $U'_{\text{BLR}}$  drops significantly (compare magenta and blue dot-dashed lines in Fig. 2b). The amount of cooling drops, shown by the appearance of a cooling break at  $10^{13}$  Hz in the magenta spectrum. Synchrotron and accretion flow seed photons become more important, broadening the Compton hump again. But even these cannot help for long;  $\dot{m} = 10^{-2}$  is the rate at which accretion flows make the transition from radiatively efficient to inefficient. Below  $\dot{m} = 10^{-2}$ , UV bright accretion discs can no longer be sustained and give way to ADAF like flows. This severely reduces the available accretion flow seed photons and effectively switches off the BLR, since there are no UV photons to illuminate it. This final magenta spectrum represents the transition from dimming FSRQ to a low accretion rate SSC BL Lac.

Fig. 2(c) shows the total energy densities of seed photons in the jet frame as a function of accretion rate. For  $-1.5 < \log \dot{m} < -0.5$ ,  $U'_{\text{BLR}}$  dominates, suppressing  $U'_{\text{sync}}$  and giving the luminous Compton hump and much smaller synchrotron peak typical of FSRQs. Only at the extremes of accretion rate does  $U'_{\text{sync}}$  dominate. At super Eddington accretion rates,  $U'_{\text{sync}}$  and  $U'_{\text{acc}}$  start to overtake  $U'_{\text{BLR}}$ , producing a pseudo-BL Lac type spectrum but with extremely high luminosity. At the lowest accretion rates,  $U'_{\text{sync}}$  recovers when  $R_{\text{BLR}}$  has shrunk below  $Z_{\text{diss}}$ , reducing the external seed photons and beginning the object's transition to a low accretion rate SSC BL Lac.

#### 4 FSRQ VISIBILITY

Having shown how the spectrum of an FSRQ might change with mass and accretion rate, we now investigate the redshift limits at which FSRQs of different masses and accretion rates should be visible to *Fermi*. We define a flux limit of  $F_{1-100 \text{ GeV}} > 5 \times 10^{-10}$  photons  $\text{cm}^{-2} \text{ s}^{-1}$  from the *Fermi* 1 year catalogue (Abdo et al. 2010). If an FSRQ of a given mass and accretion rate has  $F > F_{\text{limit}}$  in the *Fermi* band, we assume it will be detected.

Fig. 3(a) shows the redshift limits for *Fermi* visible FSRQs as a function of BH mass. We fix  $\dot{m} = 0.1$  and show three different inclination angles:  $\theta = 0$  (black),  $1/\Gamma$  (blue) and  $1/2\Gamma$  (magenta). Clearly more closely aligned FSRQs are seen out to higher redshifts. The limiting redshift increases with mass, since  $L_{\text{comp}}$  increases with mass (see Fig. 1a), until  $\sim 10^{9.6} M_{\odot}$ . A highly aligned FSRQ with a  $10^{9.5} M_{\odot}$  BH can be detected out beyond  $z = 6$ . However, above  $10^{9.5} M_{\odot}$ , the redshift limits drop sharply to  $z \leq 2$  for a  $10^{10} M_{\odot}$

BH. The reason for this can be seen in Fig. 1(a). For the most massive  $10^{10} M_{\odot}$  BHs,  $Z_{\text{diss}} > R_{\text{BLR}}$ , because  $Z_{\text{diss}}$  grows  $\propto M$ , whilst  $R_{\text{BLR}} \propto M^{1/2}$ . BLR photons are still the dominant source of seed photons; however, they are now behind the emission region. Consequently, they are deboosted, so that the peak energy of BLR seed photons is lower. This shifts the peak of the Comptonized emission to lower energies and the flux in the *Fermi* band (1–100 GeV, corresponding to  $23.38 < \log \nu < 25.38$ ) drops significantly. The luminosity of a  $10^{10} M_{\odot}$  FSRQ at  $10^{24}$  Hz is almost two orders of magnitude less than a  $10^9 M_{\odot}$  BH at the same accretion rate (compare black and blue lines, Fig. 1a). Redshifting the spectrum only exacerbates the shift of the Compton peak to lower energies and further reduces the *Fermi* flux. Consequently, the redshift limits of  $10^{10} M_{\odot}$  FSRQs are nearer to those of  $10^{7-8} M_{\odot}$  BHs.

Fig. 3(b) shows the redshift limits for FSRQs as a function of accretion rate for four different BH masses ( $M_{\text{BH}} = 10^7$  (red),  $10^8$  (magenta),  $10^9$  (blue) and  $10^{10} M_{\odot}$  (black) and  $\theta = 0$ ).  $z_{\text{limit}}$  increases with  $\dot{m}$ ; however, the rate of increase differs with mass.

The redshift limits for  $10^{7-8} M_{\odot}$  FSRQs increase very slowly with accretion rate (magenta and red lines). The redshift limit for a  $10^7 M_{\odot}$  FSRQ is  $\sim 0.5$  at  $\log \dot{m} = -2$  and  $\sim 0.75$  at  $\log \dot{m} = 1$ .  $10^8 M_{\odot}$  FSRQs show a similarly small factor of  $\sim 3$  increase over the same range in accretion rate. This is because the dominant cooling is through SSC for low-mass FSRQs, due to the small emission region size and high magnetic field. As a low-mass FSRQ ( $10^{7-8} M_{\odot}$ ) increases its accretion rate from  $\log \dot{m} = -2$  to 1, its Compton spectrum changes from being high peaked (at  $\sim 10^{24}$  Hz) to low peaked ( $\sim 10^{21}$  Hz), analogous to the change in BL Lac spectra from high peaked to low peaked. The reason is the same: increasing  $\dot{m}$  increases the cooling, shifting all the peak energies to lower frequency, because low-mass FSRQs are similarly dominated by SSC cooling (plus low energy accretion disc seed photons), which always dominates over BLR IC. Even though the total luminosity is increasing, the shift of the peak emission to lower energies means the *Fermi* band flux increases more slowly and hence  $z_{\text{limit}}$  shows a very gradual increase.

In contrast,  $10^9 M_{\odot}$  FSRQs show a much faster increase in  $z_{\text{limit}}$  with  $\dot{m}$  (blue line, Fig. 3b). This is because they are almost always dominated by BLR Compton scattering. The spectral energy density of BLR seed photons peaks at higher energy (see Fig. 1b, blue dot-dashed line) than the synchrotron and disc seed photons that dominate in lower mass systems; hence, the IC peak is at higher

energy ( $10^{23}$  compared to  $10^{20}$  Hz, compare blue and magenta lines, Fig. 1a), so more of the luminosity increase can be seen in the *Fermi* band. Only at the very lowest accretion rates ( $\log \dot{m} \sim -2$ ) does the *Fermi* visibility of a  $10^9 M_\odot$  FSRQ dip below that of a  $10^8 M_\odot$  object. This is because the Compton cooling is slightly more efficient in the larger mass object, shifting its Compton peak to slightly lower energy and hence giving it a lower *Fermi* band flux.

The  $10^{10} M_\odot$  FSRQ (black line, Fig. 3b) shows a similar effect, with  $z_{\text{limit}}$  increasing slowly at first and then more rapidly for  $\log \dot{m} > -1$ . This is because  $R_{\text{BLR}} \propto M^{1/2} \dot{m}^{1/2}$  whilst  $Z_{\text{diss}} \propto M$ , hence for larger mass a higher  $\dot{m}$  is needed for  $R_{\text{BLR}} > Z_{\text{diss}}$ , i.e.  $R_{\text{BLR}} < Z_{\text{diss}}$  up to higher  $\dot{m}$ . Whilst  $R_{\text{BLR}} < Z_{\text{diss}}$ , the IC hump is dominated by synchrotron, accretion flow and deboosted BLR seed photons, so its peak is at lower frequency and the *Fermi* band flux ( $\sim 10^{24}$  Hz) is significantly reduced. Once  $R_{\text{BLR}} > Z_{\text{diss}}$  (at  $\log \dot{m} \sim -1$  for  $M = 10^{10} M_\odot$ ), Doppler boosted BLR seed photons dominate and  $z_{\text{limit}}$  increases dramatically.

## 5 PREDICTED FSRQ POPULATION FROM COSMOLOGICAL SIMULATIONS

Combining our scaled jet emission model with the results from cosmological simulations allows us to predict the population of FSRQs that should be detected by *Fermi*. As in Paper 1, we use the BH number densities from the Millennium Simulation (Springel et al. 2005; Fanidakis et al. 2011, 2012), which predict the number of SMBHs accreting at different redshifts together with their masses and accretion rates ( $n(z, M, \dot{m})$ ). In Fig. 4, we show the luminosity density (i.e. number density multiplied by accretion luminosity) of BHs predicted by the simulation as a function of mass and accretion rate at different redshifts. The simulation has been found to agree well with the observed number densities of broad line and narrow line AGN in the local universe (Fanidakis et al. 2011, 2012).

We initially assume that all BHs accreting with  $\dot{m} > 10^{-2}$ , i.e. in the radiatively efficient regime, produce an FSRQ type jet. We can then calculate the number of AGN hosting an FSRQ jet in each  $(z, M, \dot{m})$  bin. If this number is less than 1, we use Poisson statistics to randomly determine whether a BH is present or not. Each BH in each  $(z, M, \dot{m})$  bin is then assigned a random distance within this redshift bin and random  $\theta_{\text{obs}}$ , assuming  $\cos \theta_{\text{obs}}$  is distributed uniformly. We then calculate the observed spectrum to determine whether or not the jet would be visible to *Fermi*. We choose the flux limit of the *Fermi* 1 year catalogue, in order to compare our simulation results with the observations presented in Shaw et al. (2012).

Fig. 5 shows the predicted redshift distribution of *Fermi* visible FSRQs (black line). The predicted distribution peaks between redshifts  $1 < z < 2.5$ . This corresponds to the peak in quasar activity at  $z \sim 2$ . At later times ( $z < 1$ ), typical BH accretion rates drop below  $10^{-2}$  due to systems running out of gas to accrete (Fig. 4). At low accretion rates, the accretion flow becomes radiatively inefficient and no longer produces the copious UV required to illuminate the BLR. This effectively switches off the sources of external seed photons, so that the BHs produce BL Lac rather than FSRQ type jets. A few systems remain at high accretion rates – these typically host smaller BHs ( $\sim 10^7 M_\odot$ ), which haven't yet used up their gas supplies. These correspond to Seyfert galaxies in the local Universe. According to our criteria ( $\dot{m} > 10^{-2}$ ), these BHs should host EC jets. However Fig. 3(a) shows that the *Fermi* visibility of jets

from such small BHs is poor, so their contribution to the number of FSRQs at late times ( $z < 1$ ) is small.

Whilst the predicted redshift distribution peaks at  $1 < z < 2.5$ , there is a tail out to high redshifts, with the most distant FSRQs being detected out to  $z \sim 5$ . As redshift increases, the typical BH mass decreases. At  $z = 2$ , the bulk of the accretion luminosity is produced by  $10^8 M_\odot$  BHs (Fig. 4). For  $z > 2$ , the typical BH mass producing the bulk of the accretion luminosity drops below  $10^8 M_\odot$ . Fig. 3(a) shows how sharply the *Fermi* visibility drops with mass, more than halving for a decade drop in mass from  $10^9$  to  $10^8 M_\odot$ . Fig. 3(b) shows that for small BH mass ( $\leq 10^8 M_\odot$ ), the increase in accretion rate at early times does not compensate for the drop in mass in terms of *Fermi* visibility (compare magenta and blue lines, Fig. 3b). The decreasing tail of the predicted redshift distribution from  $2.5 < z < 5$  is therefore due to the decreasing number density of  $10^{8-9} M_\odot$  BHs and the increasing reliance on strongly beamed sources ( $\theta_{\text{obs}} \sim 0$ ) to reach the *Fermi* flux limit.

The total number of *Fermi* visible FSRQs predicted by our simulation is  $\sim 26\,000$ , whilst the actual number of FSRQs detected in the *Fermi* 1 year catalogue is  $\sim 300$  (Abdo et al. 2010). Our simulation overpredicts the number of *Fermi* visible FSRQs by approximately two orders of magnitude. This is one order of magnitude less than the three orders of magnitude discrepancy found in Paper 1 using the same method to predict the *Fermi* population of BL Lacs. Nevertheless, a two order of magnitude discrepancy is still too large to be explained by the sky coverage limit of *Fermi* ( $|b| > 10^\circ$  implying 80 per cent of the sky is included). In Fig. 5, we also show the observed redshift distribution of *Fermi*-detected FSRQs from Shaw et al. (2012) (red line). The observed redshift distribution peaks at later times ( $0.5 < z < 1.5$  rather than  $1 < z < 2.5$ ), with no FSRQs detected in the 1 LAT catalogue with  $z > 3.5$ . Not only is the total number of FSRQs overpredicted, but the shape of the redshift distribution also does not match the observations.

Figs 6(c) and (d) show the predicted mass and accretion rate distributions of *Fermi* visible FSRQs from the simulation, compared to the observed distributions (Figs 6a and b) measured by Shaw et al. (2012). The typical predicted FSRQ accretion rate is  $-1 < \log \dot{m} < 0$ , since *Fermi* visibility increases with accretion rate. Above Eddington, the increase in *Fermi* flux with  $\dot{m}$  becomes progressively less (see Fig. 2a) and the number density of super Eddington sources of sufficient mass ( $> 10^8 M_\odot$ ) drops off sharply, both of which result in the typical FSRQ accretion rate being just sub-Eddington. This is in rough agreement with the findings of Shaw et al. (2012), where most FSRQs are observed to have  $-1 < \log \dot{m} < 0.5$ . The typical predicted mass is  $10^{8-8.5} M_\odot$ , since these FSRQs are bright in the *Fermi* band and most numerous at  $1 < z < 2$  where quasar activity peaks. The results of Shaw et al. (2012) show that the observed distribution is less sharply peaked and the peak extends to slightly higher mass ( $10^{8-9} M_\odot$ ).

### 5.1 Dependence on BH spin?

By assuming that every BH accreting with  $\dot{m} > 10^{-2}$  is capable of producing an FSRQ jet, our simulation overpredicts the number of *Fermi*-detected FSRQs by two orders of magnitude. Clearly another factor is reducing the number of FSRQs detected by *Fermi*. Paper 1 found that the number of *Fermi*-detected BL Lacs was similarly overpredicted (by three orders of magnitude) when the same technique was applied to predict the observed population of BL Lacs (i.e. all BHs accreting below  $10^{-2}$  produce BL Lac type jets). Paper 1 found that the observed numbers of BL Lacs, and their

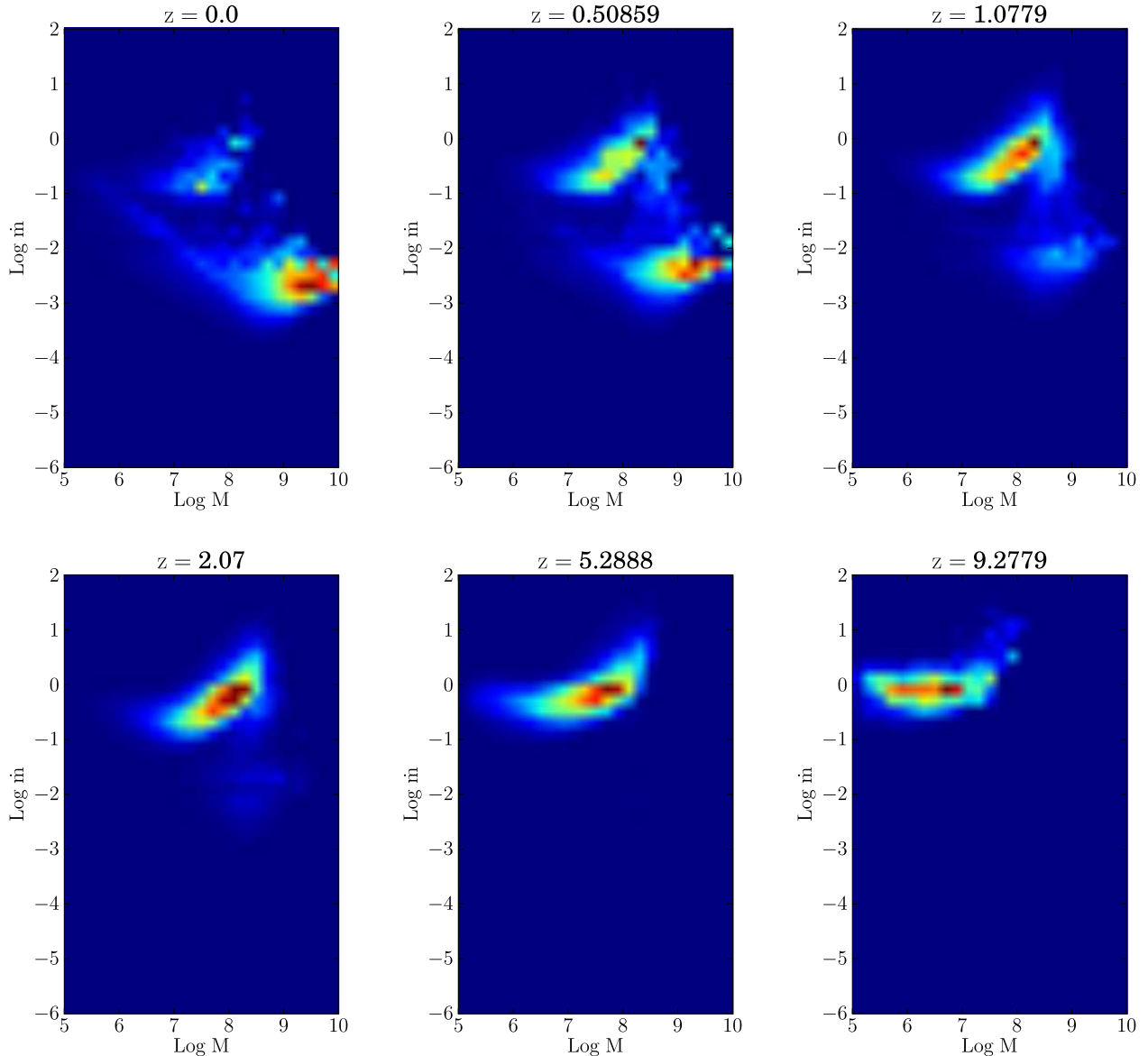


**Figure 4.** Predicted mass and accretion rate distribution of accreting BHs at increasing redshift from the Millennium simulation. Colours trace luminosity density, where we define luminosity density as the number density multiplied by the luminosity ( $L$ ) at that mass and mass accretion rate, where  $L = \eta \dot{M} c^2$  for the thin disc regime ( $10^{-2} < \dot{m} < 1$ ), joining smoothly on to a radiatively inefficient regime at lower  $\dot{m}$  where  $L \propto \dot{m}^2$  (Narayan & Yi 1995) and on to a super-Eddington flow at higher  $\dot{m}$  where  $L \propto \ln(1 + \dot{m})$  (Shakura & Sunyaev 1973). The luminosity density in each  $(z, M, \dot{m})$  bin therefore depends on the mass, accretion rate, spin (which sets  $\eta$ ), the inferred accretion regime and the number of BHs in that bin. Red shows the mass and accretion rates at which the maximum accretion luminosity is emitted at each redshift.

redshift distribution, were much better reproduced assuming that only high-spin BHs ( $a > 0.8$ ) with  $\dot{m} < 10^{-2}$  produce BL Lac type jets. This suggests BH spin might be important in the production of highly relativistic  $\Gamma = 15$  jets in BL Lacs. Maraschi et al. (2012) suggest that the efficiency of spin-powered jet production drops off sharply below 0.8, which provides additional support for an effective spin threshold for relativistic jet production at  $a \sim 0.8$  (although this is highly uncertain and there could be a more continuous distribution of jet power with spin, e.g. Tchekhovskoy, Narayan & McKinney 2010). We investigate the effect of a sharp cut-off in jet power with spin for the FSRQs in order to compare with the BL Lacs in Paper 1.

The cosmological simulations track the evolution of BH spins as well as tracking their mass and accretion rate. BH spin is affected

both by accretion and by BH–BH coalescence following galaxy mergers (Volonteri et al. 2005, 2007; Fanidakis et al. 2011, 2012). BH–BH mergers produce highly spinning BHs, as the final merged BH is spun up by the angular momentum of the orbiting merging BHs. The effect of accretion on BH spin depends on the mode of accretion. For the case of prolonged accretion, all the mass is accreted in a single event, with a single angular momentum direction, which is sufficient to spin most BHs up to maximum (Volonteri et al. 2005, 2007). If the accretion is chaotic, with gas accreted in a series of smaller events that are randomly aligned, the net angular momentum transfer to the BH is zero (King et al. 2008). Chaotic accretion therefore results in predominantly low-spin BHs, with high spins being rare and only produced by BH–BH mergers (Fanidakis et al. 2011, 2012).

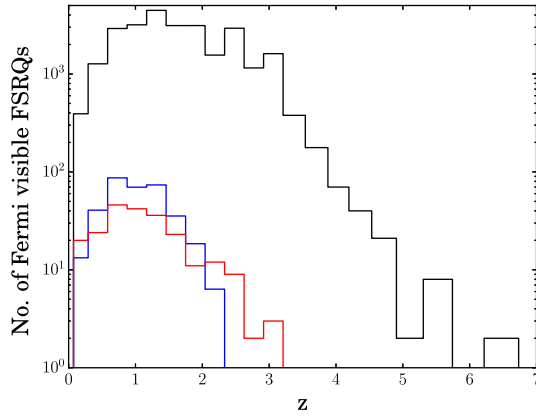


**Figure 5.** Comparison of observed and predicted FSRQ redshift distributions. Red line shows observed redshift distribution of *Fermi*-detected FSRQs found by Shaw et al. (2012). Black line shows predicted redshift distribution assuming all BHs with  $\dot{m} > 0.01$  produce an FSRQ type jet. Blue line shows predicted redshift distribution of *Fermi* visible FSRQs, assuming only BHs with  $\dot{m} > 0.01$  and spin  $a > 0.77$  produce an FSRQ type jet.

Paper 1 found the chaotic accretion model was required to match the population of *Fermi*-detected BL Lacs. High spin in the chaotic accretion model is rare, so requiring high spin reduces the predicted number of BL Lacs, in better agreement with the observed numbers. Requiring high spin also causes the predicted redshift distribution to peak at later times (lower redshift) and increases the typical predicted BL Lac mass (since gas poor mergers happen later and produce the most massive BHs), in better agreement with observations. Hence, we choose the chaotic accretion model.

The blue line in Fig. 5 shows the predicted redshift distribution of *Fermi* visible FSRQs after imposing a spin cut, so that only BHs with  $\dot{m} > 10^{-2}$  and  $a > a_{\text{cut}}$  produce an FSRQ type jet. We find  $a_{\text{cut}} \sim 0.77$  is required to reproduce the observed number of *Fermi*-detected FSRQs. However, closer comparison of the observed and predicted distributions (red and blue lines) shows that, although the total number of FSRQs is better reproduced, the simulation cannot reproduce the tail out to high redshifts ( $>2$ ). Imposing a spin cut limits the maximum expected FSRQ redshift to  $\sim 2.3$ .

Fig. 7 shows the number density of high-spin BHs ( $a > 0.8$ ) as a function of redshift from the Millennium Simulation (black line). This has two peaks, one at  $z = 0$  and one at  $z = 5$ . The red line shows the number density of high-spin BHs with low accretion rates ( $\dot{m} < 10^{-2}$ ). These are responsible for the peak at  $z = 0$ . They get their high spins from late gas poor mergers, so represent the most massive BHs. This is the population of BHs responsible for the production of BL Lac jets. The blue line shows the number density of high-spin BHs with high accretion rates ( $\dot{m} > 10^{-2}$ ). These are responsible for the peak at  $z = 5$ . They acquire their high spins through early mergers of much smaller BHs. At early times, the BHs still have a plentiful gas supply (hence their high accretion rates) and subsequent chaotic accretion gradually spins down the BHs, so that the number density of high-spin, high accretion rate BHs drops with decreasing redshift, not only because typical accretion rates drop but also because most BHs are losing their earlier high spins. If we require high spin as well as high accretion rate to produce an FSRQ type jet, then these are the BHs that should be responsible for FSRQs. However, when we include a spin cut in our simulation, our results cannot replicate the observed FSRQ population between  $2 < z < 3$ . Fig. 7 (blue line) shows that the number of high-spin,

high  $\dot{m}$  BHs has dropped significantly by  $2 < z < 3$ . Many of the high-spin BHs that remain are still small ( $10^{7-8} M_{\odot}$ ), because if they had grown significantly since their last merger the process of chaotic accretion would have reduced their spins. As a result, they are not massive enough to be *Fermi* visible in our simulation. Yet the observations show there are some relatively massive BHs with FSRQ jets at these redshifts. Our simulation accounts for spin ups due to mergers, so these BHs cannot have acquired their spins through mergers, but must have maintained them whilst growing by accretion.

This suggests that early accretion may be more organized than late accretion. Perhaps there is a transition from prolonged accretion to more chaotic accretion as gas supplies diminish and redshift decreases. In assuming a chaotic accretion mode throughout, we have therefore underestimated the number of high-spin BHs at higher redshifts ( $>2$ ), where accretion may be more ordered.

However, we know that, in order to reproduce the observed BL Lac population, most BHs must have been reduced to low spins by  $z = 2$ , when accretion rates drastically drop and chaotic accretion takes over. The problem then is, if BHs are not being spun down by chaotic accretion at early times, what causes the BHs to lose their high spins when their accretion rates drop at  $z = 2$ ?

There is one additional factor that affects BH spin, aside from accretion mode and BH–BH mergers, that the simulation does not take into account, and that is the jet itself. Powering a highly relativistic jet should cause the BH to spin down (e.g. Nemmen et al. 2007; Tchekhovskoy et al. 2011; Dotti et al. 2013). Perhaps at early times ( $z > 2$ ), when accretion is more ordered, the angular momentum the BH gains from the prolonged accretion flow balances the spin-down effect of the relativistic jet. Then, when the accretion rate drops at  $z \sim 2$ , the BH loses this input source of angular momentum and the jet spins down the BH (which in turn switches off the highly relativistic jet). A powerful jet can spin down a central BH in  $3 \times 10^8$  yr (Tchekhovskoy & McKinney 2012; Tchekhovskoy & Giannios 2015). As a result, most BHs at late times ( $z < 2$ ) are low spin and the only high-spin BHs are those which were subsequently spun up in late gas poor BH–BH mergers.

Figs 6(e) and (f) show the predicted mass and accretion rate distributions of *Fermi* visible FSRQs from our current simulation including a spin cut. Both are in clear disagreement with the observed distributions (Figs 6a and b). Imposing the spin cut has preferentially selected for low accretion rate objects ( $\dot{m}$  close to  $10^{-2}$ ), which are typically higher mass (Fig. 4). These objects are the high accretion rate end of the BL Lac population — either late mergers that were not gas poor, or BHs around  $z \sim 2$  with decreasing accretion rates that are in the process of transitioning to a radiatively inefficient accretion flow and a BL Lac type jet. Our spin cut has not captured the population of high accretion rate, relatively high-mass objects ( $10^8-10^9$ ) at  $1 < z < 3$  that make up the bulk of the observed FSRQ population. This further emphasises that a more sophisticated model combining chaotic and prolonged accretion episodes with jet spin-down is required to trace the evolution of BH spin beyond  $z = 2$ , assuming highly relativistic FSRQ jets really are a tracer of high-spin objects.

## 6 CAVEATS

The *Fermi* band flux in FSRQs is dominated by Compton upscattering of seed photons from the BLR. We have approximated the BLR as a spherical shell of radius  $R_{\text{BLR}}$  centred on the BH so that some fraction of the seed photons come from directly ahead of the jet. However, studies of line profiles have shown that the BLR

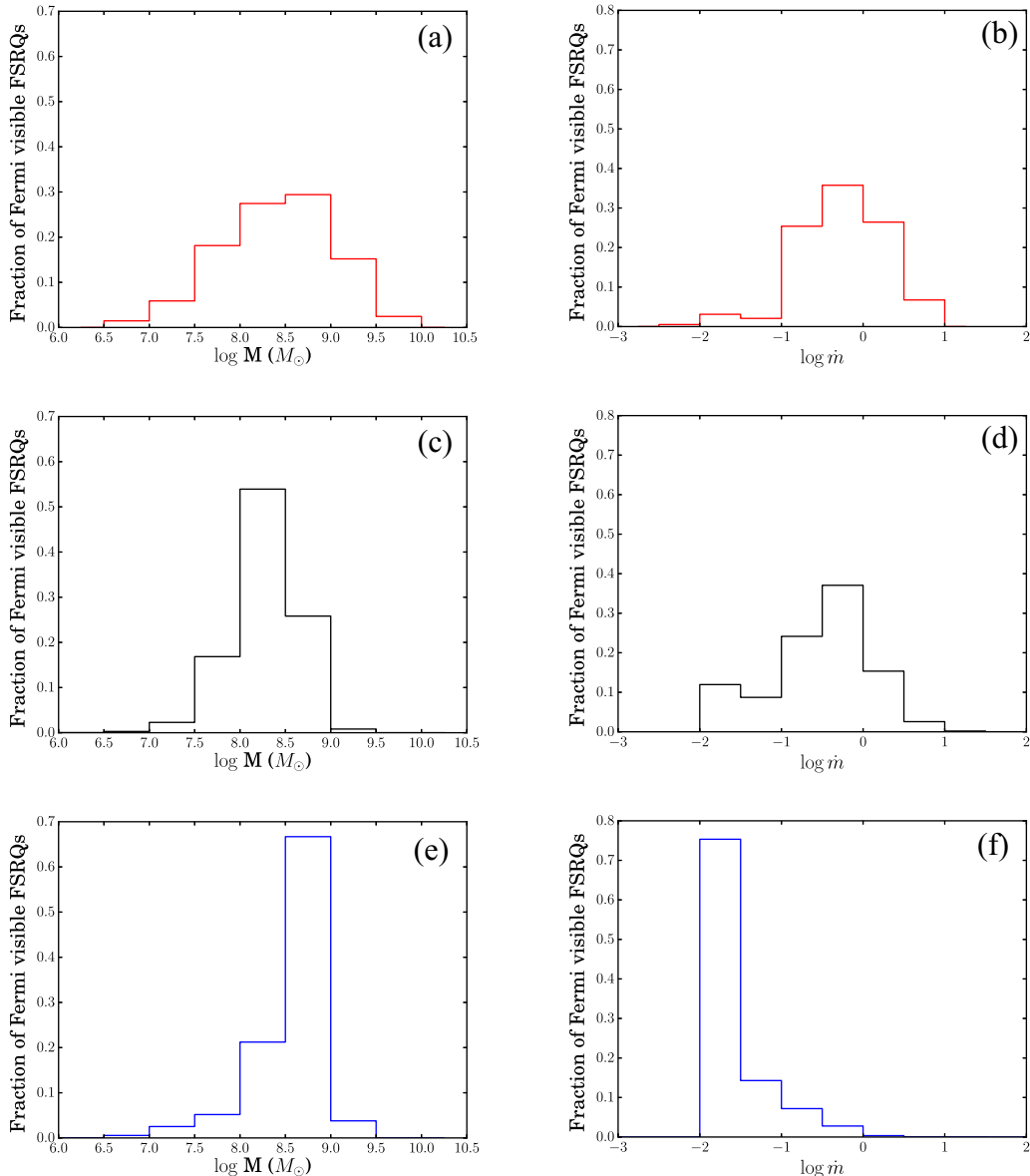


**Figure 6.** (a) and (b) show, respectively, observed mass and accretion rate distributions of *Fermi* visible FSRQs from the data of Shaw et al. (2012). (c) and (d) show predicted mass and accretion rate distributions of *Fermi* visible FSRQs assuming all BHs with  $\dot{m} > 0.01$  produce an FSRQ type jet. (e) and (f) show predicted mass and accretion rate distributions of *Fermi* visible FSRQs assuming only BHs with  $\dot{m} > 0.01$  and  $a \geq 0.77$  produce an FSRQ type jet.

geometry may be more flattened, perhaps indicating an origin as a disc wind (Kollatschny & Zetzl 2013). Nonetheless, aberration would still mean that these photons would appear close to face on in the jet frame for the bulk Lorentz factors assumed here, so this is unlikely to have much of an effect.

We have assumed that a fixed fraction of  $L_d$  is reprocessed by the BLR and torus. Again, this may not be the case. G10 find from spectral fitting of a sample of FSRQs that the fraction does vary slightly, although not by much, so this should not be important in our statistical sample.

We have used the mean FSRQ spectrum of G10 as our model spectrum from which to scale; however, FSRQs are highly variable. During flaring, the *Fermi* flux can increase by more than an order of magnitude. As a result, distant FSRQs that would not normally be detected may become visible. For example, Ghirlanda et al. (2011) note that some EGRET detected FSRQs were not visible in

the first years of *Fermi* LAT observations despite its much better sensitivity, showing that the EGRET detection was only a short flaring episode. This would extend the tail of the redshift distribution out to higher redshifts than otherwise expected. In only modelling the typical FSRQ emission, such events have not been included in our simulation.

More importantly, we have also assumed that an FSRQ jet is produced for the entire time a BH is accreting with  $\dot{m} > 10^{-2}$ . If instead the jet follows a duty cycle and is only produced for a fraction of that time, then this will reduce the number of *Fermi*-detected FSRQs. We overpredict the number of *Fermi* visible FSRQs by two orders of magnitude assuming every BH with  $\dot{m} > 10^{-2}$  produces an FSRQ jet. If each of these BHs only produces an FSRQ jet 100th of the time of each accretion episode, then we could match the observed numbers without needing any limits on the spin of the BH. However, FSRQs should be the aligned analogues of FR II sources

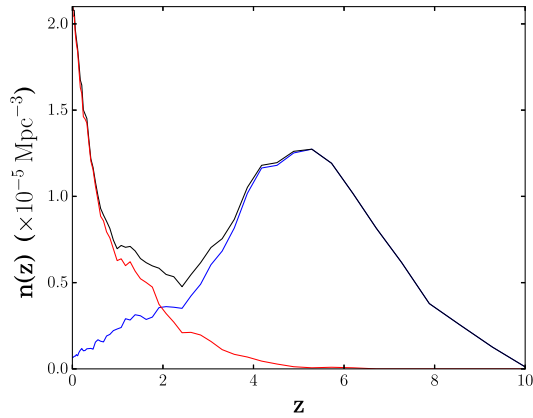


**Figure 7.** Redshift distribution of high-spin BHs ( $a > 0.8$ ) from the Millennium simulation, assuming accretion is chaotic at all redshifts. Red line shows BHs accreting with  $\dot{m} < 10^{-2}$  (corresponding to BL Lacs), blue line shows BHs accreting at  $\dot{m} > 10^{-2}$  (corresponding to FSRQs), black line shows total.

(Padovani & Urry 1992). The large-scale radio lobes of FR II sources indicate that the jet producing them must be persistent, since the time taken to produce such large-scale structures is  $\sim \text{Myr}$ , probably similar to the time of each accretion episode. One explanation may then be that the large-scale structure is produced by a persistent slower jet, whilst there is a fast central spine with  $\Gamma = 13$ , which appears as an FSRQ when viewed head on and is intermittent.

### 6.1 The gamma-ray loud NLS1 as a test of jet scalings

Our jet scalings reproduce the major trends seen in the FSRQ blazar sequence (see Sections 3.1 and 3.2). However, most of these objects are high-mass BHs. The small number of gamma-ray loud NLS1s ( $\gamma\text{NLS1s}$ ) provide a unique opportunity to test the jet scalings on much smaller mass ( $10^{6-8} M_{\odot}$ ), high accretion rate AGN. These  $\gamma\text{NLS1s}$  are a subset of the radio loud NLS1s (Komossa et al. 2006) that have been detected by *Fermi*. They show Doppler boosted jet emission with a weak synchrotron hump and strong IC emission so that their SEDs appear like ‘mini FSRQs’ (Abdo et al. 2009a, Abdo et al. 2009b). The high accretion rates of NLS1s ( $\dot{m} \sim 1$ ) mean that their accretion flows are in the radiatively efficient regime, giving them a BLR (albeit with relatively narrow broad lines), so they should correspond to low-mass FSRQs. In which case, we should be able to replicate their spectra simply by turning down the mass in our mean FSRQ spectral model.

PMN J0948+0022 was the first  $\gamma\text{NLS1}$  to be discovered. A multiwavelength monitoring campaign was carried out on the source in 2009. Abdo et al. (2009c) subsequently fitted its broad-band spectrum with the jet model of Ghisellini & Tavecchio (2009). In Table 1, we show their derived values of  $R_{\text{diss}}$ ,  $P'_{\text{rel}}$  and  $B$ . We also show the expected values of  $R_{\text{diss}}$ ,  $P'_{\text{rel}}$  and  $B$  for this source that result from scaling the mean FSRQ parameters of G10 as  $R \propto M$ ,  $P'_{\text{rel}} \propto \dot{m}M$  and  $B \propto (\dot{m}/M)^{1/2}$ , according to the mass and accretion rate of PMN J0948+0022 ( $M = 1.5 \times 10^8 M_{\odot}$ ,  $\dot{m} = 0.5$ ). These scalings correspond to assuming both the power injected into relativistic electrons and the power in magnetic fields are a fixed fraction of the accretion power, i.e.  $P'_{\text{rel}} \propto P'_B \propto P_{\text{acc}} \propto \dot{m}M$ . In Table 1, we also list the mean FSRQ values for reference.

The values of  $R_{\text{diss}}$  and  $P'_{\text{rel}}$  found from fitting the observed spectrum of PMN J0948+0022 are both slightly larger than expected from scaling from the mean FSRQ parameters. However, the biggest

**Table 1.** Comparison of the observed jet parameters for the  $\gamma\text{NLS1}$  PMN J0948+0022 (Abdo et al. 2009c) with those expected from scaling the mean FSRQ jet parameters from G10 according to standard jet scalings ( $R_{\text{diss}} \propto M$ ,  $P'_{\text{rel}} \propto \dot{m}M$ ,  $B \propto (\dot{m}/M)^{1/2}$ ).

Parameter	< FSRQ >	$\gamma\text{NLS1}$	Standard scaling prediction
$M (M_{\odot})$	$10^9$	$1.5 \times 10^8$	$1.5 \times 10^8$
$\dot{m} (L/L_{\text{Edd}})$	0.1	0.5	0.5
$R_{\text{diss}} (\times 10^{15} \text{cm})$	18.9	6.75	2.835
$P'_{\text{rel}} (\times 10^{43} \text{erg s}^{-1})$	2.0	2.3	1.5
$B (\text{G})$	2.6	4.1	15.0

difference is in the magnetic field strength. Scaling the mean FSRQ magnetic field strength of 2.6 G as  $B \propto (\dot{m}/M)^{1/2}$  implies PMN J0948+0022 should have a jet magnetic field of 15 G. In reality, the magnetic field required to fit its spectrum is much smaller (4 G). This is larger than the mean FSRQ value, as expected for its smaller mass, but not nearly as large as the standard scalings predict.

In Fig. 8, we show the effect of this on the observed spectrum. The black line shows the spectrum produced taking the mean FSRQ parameters and scaling  $R_{\text{diss}}$ ,  $P'_{\text{rel}}$  and  $B$  to the mass and accretion rate of PMN J0948+0022 according to the standard scaling relations, i.e. standard scaling prediction from Table 1. The red line shows the same spectrum, but replacing  $R_{\text{diss}}$ ,  $P'_{\text{rel}}$  and  $B$  with the values found by Abdo et al. (2009c) from fitting the observed spectrum of PMN J0948+0022 (i.e. observed values in Table 1). The red line is not a fit to PMN J0948+0022, since we have kept the other parameters ( $\phi$ ,  $\Gamma$  etc.) the same as the mean FSRQ, in order to show just the effect of correcting  $R_{\text{diss}}$ ,  $P'_{\text{rel}}$  and  $B$  (although we note that the injected electron distribution parameters of PMN J0948+0022 are not very different to those of the mean FSRQ). It is clear that replacing the values predicted by the standard scalings with the observed values has a big effect on the shape of the spectrum. The high magnetic field predicted by the standard scaling relations causes synchrotron and SSC emission to dominate the black predicted spectrum, resulting in synchrotron and Compton peaks of similar luminosity. The resulting spectral shape is similar to that of a BL Lac, where the only

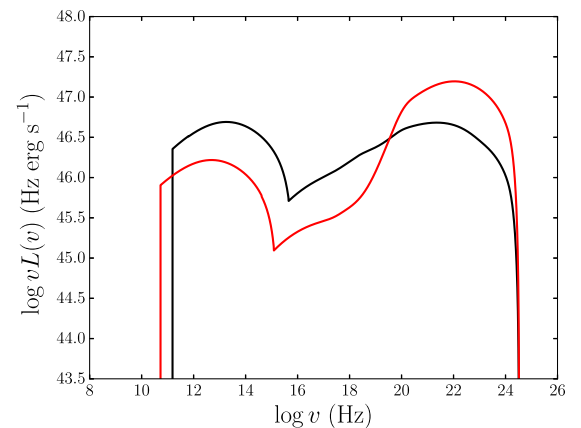


**Figure 8.** Comparison of a  $\gamma\text{NLS1}$  spectrum predicted using standard jet scalings with a spectrum using observationally constrained parameters. Black line shows expected jet spectrum for a BH with mass and accretion rate of the  $\gamma\text{NLS1}$  PMN J0948+0022 ( $M = 1.5 \times 10^8 M_{\odot}$ ,  $\dot{m} = 0.5$ ), from scaling the mean FSRQ spectrum of G10 according to standard jet scalings ( $R_{\text{diss}} \propto M$ ,  $P'_{\text{rel}} \propto \dot{m}M$  and  $B \propto (\dot{m}/M)^{1/2}$ ). Red line shows resulting spectrum replacing  $R_{\text{diss}}$ ,  $P'_{\text{rel}}$  and  $B$  with the observed values found by Abdo et al. (2009c) to fit PMN J0948+0022. See Table 1 for parameter values.

source of emission is synchrotron and SSC emission. In contrast, when we use the observed values, where the magnetic field is much lower, the Compton emission is dominated by IC from external seed photons and the synchrotron emission is suppressed (red spectrum). As a result, the Compton peak is much brighter than the synchrotron peak – a spectral shape typical of FSRQs. However, according to the standard scaling relations,  $\gamma$ NLS1s should not look like mini FSRQs – SSC should dominate their Compton humps not IC.

This leaves us with two potential scenarios. The first is that FSRQs simply do not follow standard scaling relations. This is surprising, given that these scaling relations are based on just two assumptions: that the size scales of the jet should scale with BH mass and that the power injected into relativistic electrons and the power in magnetic fields is a fixed fraction of the accretion power. Fig. 8 shows that replacing the parameters predicted by standard jet scalings with those observed for a  $\gamma$ NLS1 increases the *Fermi* flux ( $\nu \sim 10^{22}$ ) by half an order of magnitude. This suggests, if  $\gamma$ NLS1s really are low-mass versions of FSRQs, then the low-mass FSRQs in our simulation should be brighter and hence more visible than we have estimated. Consequently, our original predicted population, which already overestimates the observed population by two orders of magnitude, should be an underestimate. This only increases the need for some other factor, such as a limit on BH spin, to reduce the predicted numbers.

The alternative scenario is that FSRQs do follow standard jet scalings and the masses of  $\gamma$ NLS1s have simply been underestimated. Several studies have suggested that  $\gamma$ NLS1 masses are systematically larger, and accretion rates correspondingly lower, than previously estimated (e.g. Calderone et al. 2013; Baldi et al. 2016; D’Ammando et al. 2017). Given that  $\gamma$ NLS1s show strong Compton dominance, whereas standard jet scalings predict a low Compton dominance for typical NLS1 masses, our findings support this interpretation.

## 7 COMPARING FSRQ AND BL LAC JETS

FSRQs and BL Lacs are typically understood as representing the two ends of the ‘Blazar sequence’. The transition from low-power BL Lac to high-power FSRQ can be understood in terms of increasing accretion rate on to the central BH. The dimmest BL Lacs, produced by the lowest accretion rate BHs ( $\dot{m} < 10^{-3}$ ), appear as high-peaked BL Lacs (HBLs). Their low accretion rates mean lower magnetic fields and lower injected electron powers, which result in less cooling, so the synchrotron and SSC emission peak at high frequencies. As accretion rate increases,  $B$  and  $P'_{\text{rel}}$  increase, the amount of cooling increases, so the electron distribution cools down to lower Lorentz factors and the observed synchrotron and SSC spectra peak at lower frequencies. Increasing  $\dot{m}$ , and the corresponding increase in  $B$  and  $P'_{\text{rel}}$ , switch the observed spectrum from an HBL to a low-peaked BL Lac (LBL). As  $\dot{m}$  becomes greater than  $10^{-2}$ , the accretion flow around the BH switches from a radiatively inefficient flow to a radiatively efficient UV accretion disc, effectively turning on external sources of seed photons, and the jet stops being a BL Lac and appears as an FSRQ. In this picture, the jet is the same in both cases, the only difference is in the power input ( $B$  and  $P'_{\text{rel}}$ ) and the presence or absence of external seed photons, both of which are linked by a dependence on the accretion rate. However, in reality this is not the case. There are further differences between the two types of jet.

Comparison of the mean injected electron distribution parameters found by G10 for FSRQs and BL Lacs shows that  $\gamma_{\text{max}}$  and  $\gamma_b$  are much larger for BL Lacs ( $\gamma_{\text{max}} \sim 10^5$  for BL Lacs compared to

$10^3$  for FSRQs and  $\gamma_b \sim 10^4$  compared to  $10^2$ ). The difference between BL Lacs and FSRQs is not simply that the electrons have a different seed photon field to cool off. The accelerated electron distribution is intrinsically different in FSRQs compared to BL Lacs. This suggests there is some difference in the way electrons are accelerated, presumably by shocks, in FSRQ jets compared to BL Lacs.

A more fundamental difference is in jet opening angle ( $\phi$ ). Here and in Paper 1, we have used  $\phi = 0.1$ , which is typically assumed for calculating blazar spectra. However, Krause et al. (2012) have shown that  $\phi$  should be larger for BL Lac jets. They find from hydrodynamic simulations that jet opening angle sets the large-scale morphology of the jet, with FR II jets (corresponding to misaligned FSRQs) being produced for opening angles  $< 24^\circ$  ( $= 0.4$  rad) and FRI morphologies (corresponding to misaligned BL Lacs) being produced for larger opening angles. Since  $\phi$  relates  $Z_{\text{diss}}$  and  $R_{\text{diss}}$ , this means that the same size emission region will be located at smaller  $Z_{\text{diss}}$  for a larger opening angle. Since the calculation of BL Lac spectra does not involve any external seed photons, the only change as a result of accounting for a larger opening angle in BL Lacs will be that the  $Z_{\text{diss}}$  derived from fitting a given BL Lac spectrum will be smaller.

A related factor is that the mean BL Lac BLF is slightly larger than the mean FSRQ BLF (15 compared to 13; G10). The BLF of the jet should influence where the dissipation region is, if it corresponds to a standing shock at the base of the jet. For larger  $\Gamma$  material will travel further before shocking. The discontinuity in both opening angle and BLF suggests that  $R_{\text{diss}}$  and  $Z_{\text{diss}}$  should not scale continuously between FSRQs and BL Lacs.

## 8 CONCLUSIONS

We have combined models of FSRQ spectra together with prescriptions for how they should scale with mass and accretion rate and the number densities of BHs from cosmological simulations to predict the number of FSRQs that should be observed by *Fermi*. If we assume all BHs accreting with  $\dot{m} > 10^{-2}$  produce an FSRQ jet, our simulation overpredicts the number of *Fermi*-detected FSRQs by two orders of magnitude. If we restrict the production of FSRQ jets to high-spin BHs ( $a > 0.77$ ), we can reproduce the observed numbers. However, our predicted redshift distribution does not extend to as high redshift ( $2 < z < 3$ ) as the observed redshift distribution and we cannot match the observed mass and accretion rate distributions of FSRQs.

We suggest this may reflect a limitation in the ability of the cosmological simulations to track the evolution of BH spin. If production of FSRQ jets really does require a high-spin BH, our simulations suggest there should be more high-mass high-spin BHs at high redshift ( $\sim 2-3$ ) than a solely chaotic accretion model predicts. In a chaotic accretion model, high spin is rare and only achieved through BH–BH mergers. Therefore, the number density of high-spin BHs peaks at  $z \sim 5$  (corresponding to the first mergers of high accretion rate BHs) and  $z \sim 0$  (corresponding to late gas poor mergers of the most massive, lowest accretion rate BHs). Our simulations lack high-mass, high-spin BHs at redshift  $z = 2-3$  because chaotic accretion spins down the BHs as they grow. Yet the observed redshift distribution of FSRQs requires moderately massive ( $10^8 M_\odot$ ) BHs at  $z = 2-3$  that are high spin, assuming the FSRQ population is a tracer of high accretion rate BHs with high spin. This means these BHs must have maintained high spins whilst they were accreting, suggesting a trend from chaotic accretion (which spins down BHs) towards more prolonged accretion (which can spin up/maintain BH

spin) at high redshifts. This suggests accretion must have been more ordered in the early Universe, at least for some objects (Dotti et al. 2013; Dubois et al. 2014).

However, Paper 1 showed that, for  $z < 2$ , a chaotic accretion model is required to reproduce the observed population of BL Lacs. This means that, by  $1.5 < z < 2$ , most BHs must have been reduced to low spin, so that the only high-spin BHs in the local Universe are the most massive BHs, which have undergone late gas poor mergers. The problem then is how to explain the sudden reduction in BH spin in those objects that were previously maintaining their high spin via prolonged accretion. This loss of spin may be caused by the jet itself, since a Blandford–Znajek jet is powered by the spin energy. The resultant time-scale for spin-down depends on the balance of this extraction of spin energy with spin-up from accretion of the same material that brings in the magnetic field to power the jet (Wilson & Colbert 1995; Moderski & Sikora 1996). Whilst these objects are highly accreting at  $z > 2$ , the angular momentum the BH gains from the prolonged accretion flow balances the spin-down effect of the relativistic FSRQ jet. Then, when the accretion rate begins to drop at  $z \sim 2$ , the BH loses this input source of angular momentum and the jet spins down the BH, which in turn switches off the highly relativistic jet. A powerful jet can spin down a central BH in  $3 \times 10^8$  yr (Tchekhovskoy & McKinney 2012; Tchekhovskoy & Giannios 2015), which is sufficient to reduce most previously high-spin BHs to low spin at late times ( $z < 2$ ).

An important additional factor in our simulations are the scaling relations we use to predict the spectra from FSRQs of different masses and accretion rates. We test these by comparing our scaled models with gamma-ray loud NLS1s ( $\gamma$ NLS1s), which should be scaled down versions of the more massive FSRQs. We find that standard scaling relations (allowing all size scales to scale with mass and assuming the power injected into relativistic electrons and magnetic fields is a constant fraction of the accretion power) predict  $\gamma$ NLS1s spectra should be much less Compton dominant than observed. On face value, this suggests that, for some reason, FSRQ jets do not follow standard jet scaling relations. However, an alternative explanation may be that  $\gamma$ NLS1 masses are not as low as previously estimated. In which case, the high Compton dominance of  $\gamma$ NLS1 spectra supports the suggestion of other recent studies (e.g. Calderone et al. 2013; Baldi et al. 2016; D’Ammando et al. 2017) that  $\gamma$ NLS1 masses have been systematically underestimated.

It is clear that not every BH accreting with  $\dot{m} > 10^{-2}$  can produce an FSRQ jet, just as not every BH accreting with  $\dot{m} < 10^{-2}$  can produce a BL Lac jet. Restricting highly relativistic jet production to high-spin BHs produces a good match to the observed population of BL Lacs (Paper 1), so it is likely that high spin may be similarly important for FSRQs, whose jets appear to be the high accretion rate analogues of BL Lacs. In which case, combining the observed redshift distributions of BL Lacs and FSRQs should allow us to trace the population of high-spin BHs as a function of redshift. This provides a powerful observational constraint to test whether new models combining chaotic and prolonged accretion with jet spin-down really can track the evolution of BH spin across cosmic time.

## ACKNOWLEDGEMENTS

We thank Nikos Fanidakis and the Millennium simulation for use of their data. This work has made use of Ned Wright’s Cosmology Calculator (Wright 2006). EG acknowledges funding from the UK Science and Technology Facilities Council.

## REFERENCES

- Abdo A. A. et al., 2009a, *ApJ*, 699, 976  
 Abdo A. A. et al., 2009b, *ApJ*, 707, L142  
 Abdo A. A. et al., 2009c, *ApJ*, 707, 727  
 Abdo A. A. et al., 2010, *ApJ*, 715, 429  
 Baldi R. D., Capetti A., Robinson A., Laor A., Behar E., 2016, *MNRAS*, 458, L69  
 Blandford R. D., Znajek R. L., 1977, *MNRAS*, 179, 433  
 Calderone G., Ghisellini G., Colpi M., Dotti M., 2013, *MNRAS*, 431, 210  
 D’Ammando F., Acosta-Pulido J. A., Capetti A., Raiteri C. M., Baldi R. D., Orienti M., Ramos Almeida C., 2017, *MNRAS*, 469, L11  
 Dermer C. D., Menon M., 2009, *High Energy Radiation from Black Holes: Gamma Rays, Cosmic Rays, and Neutrinos*. Princeton University Press, NJ  
 Done C., Gierliński M., Kubota A., 2007, *A&A Rev.*, 15, 1  
 Dotti M., Colpi M., Pallini S., Perego A., Volonteri M., 2013, *ApJ*, 762, 68  
 Dubois Y., Volonteri M., Silk J., 2014, *MNRAS*, 440, 1590  
 Fanidakis N., Baugh C. M., Benson A. J., Bower R. G., Cole S., Done C., Frenk C. S., 2011, *MNRAS*, 410, 53  
 Fanidakis N. et al., 2012, *MNRAS*, 419, 2797  
 Fossati G., Maraschi L., Celotti A., Comastri A., Ghisellini G., 1998, *MNRAS*, 299, 433  
 Gardner E., Done C., 2014, *MNRAS*, 438, 779 (Paper 1)  
 Ghirlanda G., Ghisellini G., Tavecchio F., Foschini L., Bonnoli G., 2011, *MNRAS*, 413, 852  
 Ghisellini G., Tavecchio F., 2009, *MNRAS*, 397, 985  
 Ghisellini G., Maraschi L., Treves A., 1985, *A&A*, 146, 204  
 Ghisellini G., George I. M., Done C., 1989, *MNRAS*, 241, 43P  
 Ghisellini G., George I. M., Fabian A. C., Done C., 1991, *MNRAS*, 248, 14  
 Ghisellini G., Maraschi L., Tavecchio F., 2009, *MNRAS*, 396, L105  
 Ghisellini G., Tavecchio F., Foschini L., Ghirlanda G., Maraschi L., Celotti A., 2010, *MNRAS*, 402, 497 (G10)  
 Ghisellini G., Tavecchio F., Maraschi L., Celotti A., Sbarrato T., 2014, *Nature*, 515, 376  
 Ghisellini G., Righi C., Costamante L., Tavecchio F., 2017, *MNRAS*, 469, 255  
 Gierliński M., Zdziarski A. A., Poutanen J., Coppi P. S., Ebisawa K., Johnson W. N., 1999, *MNRAS*, 309, 496  
 Giommi P., Padovani P., Polenta G., Turriziani S., D’Elia V., Piranomonte S., 2012, *MNRAS*, 420, 2899  
 Heinz S., Sunyaev R. A., 2003, *MNRAS*, 343, L59  
 King A. R., Pringle J. E., Hofmann J. A., 2008, *MNRAS*, 385, 1621  
 Kollatschny W., Zetzl M., 2013, *A&A*, 558, AA26  
 Komossa S., Voges W., Xu D., Mathur S., Adorf H.-M., Lemson G., Duschl W. J., Grupe D., 2006, *AJ*, 132, 531  
 Krause M., Alexander P., Riley J., Hopton D., 2012, *MNRAS*, 427, 3196  
 Maraschi L., Colpi M., Ghisellini G., Perego A., Tavecchio F., 2012, *JPhCS*, 355, 012016  
 Moderski R., Sikora M., 1996, *MNRAS*, 283, 854  
 Moderski R., Sikora M., Lasota J.-P., 1998, *MNRAS*, 301, 142  
 Narayan R., Yi I., 1995, *ApJ*, 452, 710  
 Nemmen R. S., Bower R. G., Babul A., Storchi-Bergmann T., 2007, *MNRAS*, 377, 1652  
 Nolan P. L. et al., 2012, *ApJS*, 199, 31  
 Padovani P., Urry C. M., 1992, *ApJ*, 387, 449  
 Padovani P., Bonzini M., Kellermann K. I., Miller N., Mainieri V., Tozzi P., 2015, *MNRAS*, 452, 1263  
 Shakura N. I., Sunyaev R. A., 1973, *A&A*, 24, 337  
 Shaw M. S. et al., 2012, *ApJ*, 748, 49  
 Springel V. et al., 2005, *Nature*, 435, 629  
 Stickel M., Padovani P., Urry C. M., Fried J. W., Kuehr H., 1991, *ApJ*, 374, 431  
 Tchekhovskoy A., Giannios D., 2015, *MNRAS*, 447, 327  
 Tchekhovskoy A., McKinney J. C., 2012, *MNRAS*, 423, L55  
 Tchekhovskoy A., Narayan R., McKinney J. C., 2010, *ApJ*, 711, 50  
 Tchekhovskoy A., Narayan R., McKinney J. C., 2011, *MNRAS*, 418, L79  
 Volonteri M., Madau P., Quataert E., Rees M. J., 2005, *ApJ*, 620, 69

Volonteri M., Sikora M., Lasota J.-P., 2007, *ApJ*, 667, 704  
 Wilson A. S., Colbert E. J. M., 1995, *ApJ*, 438, 62  
 Wright E. L., 2006, *PASP*, 118, 1711

## APPENDIX

The jet emission model is publicly available as the `XSPEC` local model `JET`. This is the single zone, leptonic, relativistic jet model developed by Ghisellini & Tavecchio (2009), as used in Ghisellini et al. (2010), as coded up by Gardner and Done for this work. Please reference all three papers if you use this model in `XSPEC`. It can be used in conjunction with `OPTXAGNF`, which models the emission from the accretion flow. In which case, the first three parameters (BH mass, comoving distance and accretion rate) can be tied together.

Table A1 lists the model parameters. The first three set the parameters of the BH and the distance. Parameters 4–7 set the physical parameters of the jet: inclination to the line of sight, BLF, jet opening angle and distance of the emission region from the BH. When combined together the last two of these set the radius of the emission region, since the code assumes a conical jet. Parameters 8 and 9 set the jet magnetic field and the power injected into relativistic electrons. Parameters 10–14 determine the shape of the injected electron distribution, and parameter 15 sets the redshift. `XSPEC` requires a 16th normalization parameter, which must be fixed at unity.

The code can be used to model both FSRQs and BL Lacs. If  $\log \dot{m} < -2$  (parameter 3), the code assumes the accretion flow regime is radiatively inefficient and there is no UV bright accretion disc. In this case, the external seed photon energy density is set to zero and the model calculates only synchrotron and SSC emission, producing a BL Lac type jet. If  $\log \dot{m} \geq -2$ , then the model assumes a radiatively efficient accretion disc is present and it includes IC emission from external sources of seed photons by assuming the radiatively efficient disc illuminates the BLR and torus, both of which reprocess a fraction of the disc emission. In this case, the code calculates the energy density of seed photons from direct disc and coronal emission, BLR emission, reflection of coronal X-rays off the BLR and emission from the torus, following the method of Ghisellini & Tavecchio (2009).

The code prints to screen which type of jet is calculated (SSC or SSC+IC), along with the logarithm of the power in radiation, magnetic fields, electrons, protons and total jet power ( $P_r$ ,  $P_B$ ,  $P_e$ ,  $P_p$  and  $P_j$ ), where all five powers are in the observer's frame. For SSC+IC jets, the code prints to screen  $R_{\text{BLR}}$  and  $R_{\text{IR}}$  and flags if  $Z_{\text{diss}} > R_{\text{BLR}}$  and  $Z_{\text{diss}} > R_{\text{IR}}$ .

The various spectral components (synchrotron, SSC, EC disc, EC X-ray corona, EC BLR, EC X-ray reflection from BLR and EC torus) can be written out individually, by editing the code and uncommenting the six lines beginning `WRITE(2,*)`. This produces file `fort.2` in the directory where `XSPEC` is being run. Uncommenting the lines beginning `WRITE(3,*)` writes out the energy density of seed photons in the jet frame ( $U'(v')$ ) in file `fort.3`, writing out in order: disc, coronal, BLR, reflected coronal X-rays and torus seed photon energy densities (if including IC) and, lastly, the energy density of synchrotron seed photons. Uncommenting the line beginning `WRITE(908,*)` will write the steady state electron distribution ( $N(\gamma)$ ) to `fort.908`.

Since the inclination of the jet is a parameter, the code can in practice be used to model any jet, not just highly aligned blazars. However, the code assumes a single emission zone, so it is best suited for modelling the high energy jet base emission. Although the `FORTRAN` subroutine can be easily modified to be called multiple

**Table A1.** Summary of the `JET` model parameters.

Parameter	Description	
1	$M$	BH mass in solar masses
2	$R_{co}$	Comoving distance in Mpc
3	$\log \dot{m}$	Logarithm of mass accretion rate in units of $L/L_{\text{Edd}}$ (if $\log \dot{m} < -2$ , code does SSC with no external seed photons)
4	$\theta_{\text{obs}}$	Inclination of jet axis from line of sight in degrees
5	$\Gamma$	Jet bulk Lorentz factor
6	$\phi$	Jet opening angle in radians
7	$z_{\text{diss}}$	Distance of dissipation region from BH in $R_g$ (radius of dissipation region, $r_{\text{diss}} = \phi z_{\text{diss}}$ )
8	$B$	Magnetic field in Gauss
9	$\log P'_{\text{rel}}$	Power injected into relativistic electrons in the jet frame in $\text{erg s}^{-1}$
10	$\gamma_{\text{min}}$	Minimum Lorentz factor of injected electron distribution
11	$\gamma_b$	Lorentz factor of break in injected electron distribution
12	$\gamma_{\text{max}}$	Maximum Lorentz factor of injected electron distribution
13	$s_1$	Index of injected electron distribution below the break
14	$s_2$	Index of injected electron distribution above the break
15	$z$	Redshift
16	Norm	Normalization – must be fixed at unity

times with increasing emission region size to model more extended structures.

## A1 Jet emission calculation

The emission comes from a single spherical zone of radius  $R_{\text{diss}}$ . We assume the jet has a constant opening angle ( $\phi$ ), such that the distance of the emission region from the central BH ( $Z_{\text{diss}} = z_{\text{diss}} R_g$ ) is related to the radius of the emission region by  $R_{\text{diss}} = \phi Z_{\text{diss}}$ . We assume material in the jet moves at a constant bulk Lorentz factor ( $\Gamma$ ) and that some fraction of the transported electrons are accelerated into a power-law distribution between minimum and maximum Lorentz factors  $\gamma_{\text{min}}$  and  $\gamma_{\text{max}}$ , of the form:

$$Q(\gamma) = Q_0 \frac{\left(\frac{\gamma}{\gamma_b}\right)^{-s_1}}{\left[1 + \left(\frac{\gamma}{\gamma_b}\right)^{-s_1+s_2}\right]} = Q_0 q(\gamma) \quad \text{for } \gamma_{\text{min}} < \gamma < \gamma_{\text{max}}, \quad (\text{A1})$$

where  $\gamma_b$  is the Lorentz factor at which the electron distribution changes in slope from  $s_1$  to  $s_2$ . We calculate the normalization  $Q_0$  from the power injected into the accelerated electrons ( $P'_{\text{rel}}$ ):

$$P'_{\text{rel}} = \frac{4\pi}{3} R_{\text{diss}}^3 m_e c^2 Q_0 \int_{\gamma_{\text{min}}}^{\gamma_{\text{max}}} \gamma q(\gamma) d\gamma. \quad (\text{A2})$$

We calculate  $\gamma_{\text{cool}}$  after a light crossing time  $t_{\text{cross}} = R_{\text{diss}}/c = \gamma_{\text{cool}}/\dot{\gamma}_{\text{cool}}$ , as

$$\gamma_{\text{cool}} = \frac{3m_e c^2}{4\sigma_T R U'_{\text{seed}}}, \quad (\text{A3})$$

where  $U'_{\text{seed}} = U'_B + U'_{\text{sync}} + U'_{\text{ex}}$  is the sum of the energy density in magnetic fields, synchrotron emission and external emission that provides the seed photons for cooling.

We solve the continuity equation to find the self-consistent steady-state electron distribution:

$$N(\gamma, t_{\text{cross}}) = Kn(\gamma) = \begin{cases} A Q_0 q(\gamma) & \text{for } \gamma_{\text{min}} < \gamma < \gamma_{\text{cool}} \\ \frac{3m_e c^2}{4\sigma_T c U'_{\text{seed}}} \frac{Q_0}{\gamma^2} \int_{\gamma}^{\gamma_{\text{max}}} q(\gamma_i) d\gamma_i & \text{for } \gamma_{\text{cool}} < \gamma < \gamma_{\text{max}}, \end{cases} \quad (\text{A4})$$

where  $A$  is found by matching at  $\gamma_{\text{cool}}$ .

We use the delta function approximation and calculate the synchrotron emissivity as

$$j'_{\text{sync}}(v') = \frac{\sigma_T c}{6\pi v'_B} U'_B \gamma N(\gamma), \quad (\text{A5})$$

where the electron Lorentz factor and synchrotron photon frequency are related by  $\gamma = \sqrt{3v'/4v'_B}$  and we calculate the synchrotron self-absorption frequency ( $v'_{\text{ssa}}$ ) as given by Ghisellini, Maraschi & Treves (1985):

$$v'_{\text{ssa}} = \left( 4.62 \times 10^{14} K B^{2.5} \frac{R_{\text{diss}}}{0.7} \right)^{2/7}. \quad (\text{A6})$$

We calculate Compton emission including the Klein–Nishina cross-section using the delta approximation:

$$j'_{\text{comp}}(v') = \frac{\sigma_T c}{6\pi} \int_{\gamma_{\text{min}}}^{\gamma_{\text{max}}} \int_{v'_{\text{seed, min}}}^{v'_{\text{seed, max}}} \frac{U'_{\text{seed}}(v'_{\text{seed}})}{v'_{\text{seed}}} \gamma N(\gamma) dv'_{\text{seed}} d\gamma, \quad (\text{A7})$$

where the electron Lorentz factor and Compton photon frequency are related by  $\gamma = \sqrt{3v'/4v'_{\text{seed}}}$ .

Bulk motion of the jet boosts and blue shifts the emission. We calculate the observed flux as

$$F(v'\delta/(1+z)) = \frac{(j'_{\text{sync}}(v') + j'_{\text{comp}}(v'))}{R_{\text{co}}^2} \frac{4\pi}{3} R_{\text{diss}}^3 \delta^3, \quad (\text{A8})$$

where  $\delta = (\Gamma - \cos\theta\sqrt{\Gamma^2 - 1})^{-1}$  is the Doppler factor and  $R_{\text{co}}$  is the comoving distance to the object at redshift  $z$ .

We neglect photon–photon pair production. However, the code calculates the source compactness and flags a warning if  $l' \geq 30$ . This corresponds to  $\tau_{\gamma\gamma} \sim 1$ , i.e. when the source starts to become optically thick to photon–photon pair production and this effect becomes important. For most blazar jets, the compactness is typically  $< 3$ .

## A2 External seed photons

If  $\log \dot{m} \geq -2$ , the model assumes a radiatively efficient accretion disc is present and includes IC emission from external sources of seed photons, calculating the energy density of seed photons following the method of Ghisellini & Tavecchio (2009). The model includes direct disc and coronal emission, BLR emission, reflection of coronal X-rays off the BLR and emission from the torus.

The accretion disc luminosity ( $L_d$ ) is calculated from  $M$  and  $\dot{m}$  (parameters 1 and 3). Each annulus of the disc is seen at a different angle with respect to the jet emission region, so receives a difference amount of Doppler deboosting ( $b_d$ ). We approximate the energy density of disc seed photons from each annulus in the jet frame as

$$U'_d(v') = \frac{4\pi h b_d}{c^3} \frac{(v'/b_d)^3}{\exp\left[\frac{hv'/b_d}{kT}\right] - 1} d\mu_d, \quad (\text{A9})$$

where  $b_d = \Gamma(1 - \beta\mu_d)$ ,  $\mu_d = \cos\eta$  and  $\eta$  is the angle of the annulus with respect to the jet axis.  $\mu_d$  therefore varies between

$\mu_{\text{max}} = 1$ , for the innermost radii that are directly behind the jet and experience most deboosting, to  $\mu_{\text{min}} = [1 + (R_{d,\text{max}}/Z_{\text{diss}})^2]^{-1/2}$  for the outermost radius  $R_{d,\text{max}} = 1000R_g$ . We calculate the temperature of each disc radius from the mass and accretion rate input in parameters 1 and 3.

We assume the luminosity of coronal X-rays is  $L_X = f_X L_d = 0.1L_d$  and the corona extends to  $R_X = 60R_g$ . Its emission is therefore deboosted by a factor  $b_X = \Gamma(1 - \beta\mu_X)$ , where  $\mu_X = [1 + (R_X/Z_{\text{diss}})^2]^{-1/2}$ . The total energy density of coronal seed photons in the jet frame is therefore

$$U'_X = \frac{f_X L_d \Gamma^2}{\pi R_X^2 c} \left[ 1 - \mu_X - \beta(1 - \mu_X^2) + \frac{\beta^2}{3}(1 - \mu_X^3) \right]. \quad (\text{A10})$$

We assume the spectrum of this emission is a power-law cut-off starting from  $b_X v_{d,\text{peak}}$  in the jet frame, where  $v_{d,\text{peak}} = 4kT_{\text{max}}/h$  is the frequency at which the unboosted disc spectrum peaks. We assume the power-law cut-off  $\nu_c = 150 \times 10^3 e/h$ , so that

$$U'_X(v') \propto v'^{-\alpha_X} \exp\left[-\frac{v'}{b_X \nu_c}\right], \quad (\text{A11})$$

where  $\alpha = 1$ .

We assume a fraction  $f_{\text{BLR}} = 0.1$  of the disc luminosity is reprocessed by the BLR. This emission takes the form of a BB centred on the frequency of the Lyman  $\alpha$  line ( $\nu_{\text{Ly}\alpha} = \frac{c}{4(1216 \times 10^{-8})}$ ), so that

$$U'_{\text{BLR}}(v') \propto \frac{v'^3}{\exp\left[\frac{v'}{b_{\text{BLR}} \nu_{\text{Ly}\alpha}}\right] - 1}. \quad (\text{A12})$$

The total energy density in the jet frame ( $U'_{\text{BLR}}$ ) and boosting factor ( $b_{\text{BLR}}$ ) depend on the radius of the BLR ( $R_{\text{BLR}}$ ) compared to  $Z_{\text{diss}}$ . The radius of the BLR scales with  $L_d$  as

$$R_{\text{BLR}} = 10^{17} \left( \frac{L_d}{10^{45} \text{erg s}^{-1}} \right)^{1/2} \text{cm}. \quad (\text{A13})$$

If  $Z_{\text{diss}} < R_{\text{BLR}}$ :

$$U'_{\text{BLR}} = \frac{17\Gamma^2}{12} \frac{f_{\text{BLR}} L_d}{4\pi c R_{\text{BLR}}^2} \quad (\text{A14})$$

$$b_{\text{BLR}} = \Gamma. \quad (\text{A15})$$

If  $Z_{\text{diss}} > 3R_{\text{BLR}}$ :

$$U'_{\text{BLR}} = \frac{f_{\text{BLR}} L_d}{4\pi c R_{\text{BLR}}^2} \frac{\Gamma^2}{3\beta} \left[ 2(1 - \beta\mu_1)^3 - (1 - \beta\mu_2)^3 - (1 - \beta)^3 \right] \quad (\text{A16})$$

$$\mu_1 = [1 + (R_{\text{BLR}}/Z_{\text{diss}})^2]^{-1/2} \quad (\text{A17})$$

$$\mu_2 = [1 - (R_{\text{BLR}}/Z_{\text{diss}})^2]^{1/2} \quad (\text{A18})$$

$$b_{\text{BLR}} = \Gamma(1 - \beta\mu_1). \quad (\text{A19})$$

If  $R_{\text{BLR}} \leq Z_{\text{diss}} \leq 3R_{\text{BLR}}$ , we use a power-law interpolation between the two regimes for  $U'_{\text{BLR}}$  and use  $b_{\text{BLR}} = \Gamma(1 - \beta\mu_1)$  for  $Z_{\text{diss}} = 3R_{\text{BLR}}$ .

We assume a fraction  $f_{\text{XBLR}} = 0.01$  of the coronal X-rays are reflected by the BLR clouds. We assume the reflected emission has the same cut-off power-law shape as the direct coronal emission.

Both  $b_{\text{XBRL}}$  and  $U'_{\text{XBRL}}$  vary as  $b_{\text{BLR}}$  and  $U'_{\text{BLR}}$ , with  $f_{\text{BLR}}L_d$  replaced with  $f_{\text{XBRL}}f_XL_d$ .

We assume a fraction  $f_{\text{IR}} = 0.3$  of the disc luminosity is reprocessed by the torus. This emission takes the form of a BB at  $\sim 370\text{K}$  (i.e.  $\nu_{\text{IR}} = 370k/h$ ), so that

$$U'_{\text{IR}}(\nu') \propto \frac{\nu'^3}{\exp\left[\frac{\nu'}{b_{\text{IR}}\nu_{\text{IR}}}\right] - 1}. \quad (\text{A20})$$

As in the case of the BLR seed photons,  $U'_{\text{IR}}$  and  $b_{\text{IR}}$  depend on the radius of the torus ( $R_{\text{IR}}$ ) compared to  $Z_{\text{diss}}$ .  $R_{\text{IR}}$  scales with  $L_d$  as

$$R_{\text{IR}} = 2.5 \times 10^{18} \left(\frac{L_d}{10^{45} \text{ erg s}^{-1}}\right)^{1/2} \text{ cm} \quad (\text{A21})$$

and again we consider three regimes. If  $Z_{\text{diss}} < R_{\text{IR}}$ :

$$U'_{\text{IR}} = \frac{f_{\text{IR}}L_d\Gamma^2}{4\pi c R_{\text{IR}}^2}. \quad (\text{A22})$$

If  $Z_{\text{diss}} > 3R_{\text{IR}}$ :

$$U'_{\text{IR}} = \frac{f_{\text{IR}}L_d}{4\pi c R_{\text{IR}}^2} \frac{\Gamma^2}{3\beta} [2(1 - \beta\mu_1)^3 - (1 - \beta\mu_2)^3 - (1 - \beta)^3] \quad (\text{A23})$$

$$\mu_1 = [1 + (R_{\text{IR}}/Z_{\text{diss}})^2]^{-1/2} \quad (\text{A24})$$

$$\mu_2 = [1 - (R_{\text{IR}}/Z_{\text{diss}})^2]^{1/2}. \quad (\text{A25})$$

If  $R_{\text{IR}} \leq Z_{\text{diss}} \leq 3R_{\text{IR}}$ , we use a power-law interpolation between the two regimes for  $U'_{\text{IR}}$ . In all three cases, we use  $b_{\text{IR}} = \Gamma(1 - \beta\mu_{\text{IR}})$ , where  $\mu_{\text{IR}} = \cos(\arctan(R_{\text{IR}}/Z_{\text{diss}}))$ .

This paper has been typeset from a  $\text{\TeX}/\text{\LaTeX}$  file prepared by the author.